MÖSSBAUER AND TRIBOLOGICAL STUDIES OF NITROGEN IMPLANTED AUSTENITIC STAINLESS STEELS

by

Li Wang

ProQuest LLC.
789 East Eisenhower Parkway
P.O. Box 1346
Ann Arbor, MI 48106 – 1346

T-3789

A thesis submitted to the Faculty and the Board of Trustees of the Colorado School of Mines in partial fulfillment of the requirements for the degree of master of science (Physics).

Golden, Colorado
Date: 1/12/90

Signed: Li Wang
Li Wang

Golden, Colorado
Date: 1/12/90

Approved: Don L. Williamson

Dr. Don L. Williamson
Thesis Advisor

Golden, Colorado
Date: 1/10/90

Dr. F. D. Schowengerdt
Head of Physics Dept.

Abstract

Type AISI 304 and 310 stainless steels were implanted with 60 keV nitrogen ions with doses ranging from 0.5 X 10^{17} ions/cm^2 to 10 X 10^{17} ions/cm^2 and at temperatures from 160°C to 400°C. Conversion electron Mössbauer spectroscopy and X-ray diffraction were used to determine the near-surface microstructural alterations resulting from nitrogen implantation. Auger electron spectroscopy provided implanted nitrogen concentrations as a function of depth. Results were carefully correlated with wear tests and microhardness measurements made on the same samples. Dramatic improvement in wear resistance and surface hardness occurred when the implantation was done at 380°C to the highest doses and this was found to be due to a very deep penetration (from 0.2 μm to 1.6 μm) of N to form a thick layer that is strengthened by large concentrations (from 7.5 at.% to 20 at.%) of N in solid solution. In addition, it was found that austenite transformed to martensite in unimplanted samples during polishing and wear testing. A reverse transformation to austenite occurred during implantation. However, the role of martensite in the wear behavior of implanted samples was found to be unimportant.

TABLE OF CONTENTS

LIST OF FIGURES

LIST OF TABLES

Acknowledgments

I gratefully acknowledge the contributions of my advisor Dr. Don L. Williamson. Without his endless patience, and willing help, this dissertation would still be a dream.

I would like to express my special thanks to Dr. F. E. Cecil and Dr. T. E. Furtak for serving on my committee.

Thanks are also due to Mr. Yi Qu , Mr. Kevin Kalmbach, and my husband, Dahong Du, from the Colorado School of Mines, Dr. P. J. Wilbur, Mr. Ronghua Wei, and Dr. W. S. Sampath from Colorado State University for their cooperation.

Special thanks go to my parents, for their encouragement and sacrifice. Finally, I wish to thank all of the members of the Physics Department at the Colorado School of Mines.

1. INTRODUCTION

Tribology is the study of the behavior of materials in rubbing contact. Tribological characteristics include the hardness, the friction coefficient, the wear rate and the topography of the wear tracks. Since these characteristics are surface sensitive, any modification of the surface properties can be examined by studying these tribological characteristics. It is recognized that friction and wear are not intrinsic material properties but are characteristics of the engineering system, so understanding tribological characteristics is especially important in the engineering of materials.

For over a decade, the method of ion implantation has been developed to improve tribological properties. Ion implantation is a unique method for altering the near-surface chemical composition and microstructure of materials. This method has several advantages and disadvantages in comparison with other surface modification techniques. The main advantages are [1]: it is a non-equilibrium process so that any element can be incorporated into any solid; lower processing temperature, a uniform modification depth, and negligible structural distortion. The disadvantages are: the high capital cost, the shallow penetration depth and that it is a line-of-sight process.

While surface property improvement by ion implantation has been shown in many materials, the mechanisms responsible are still poorly understood.

The materials under investigation by our group (Colorado State

University, CSU, and Colorado School of Mines, CSM) are pure iron (99.9985%), stainless steel (SS) (AISI-304 and 310), and carbon steel (0.4% carbon). For the pure iron studies [2], nitrogen and argon were implanted. Wear tests were done at CSU by using a unique oscillating pin-on-disc test machine [3]. It has been shown that mild adhesive wear resistance increased dramatically after nitrogen ion implantation into pure iron. The backscatter Mössbauer techniques of conversion electron Mössbauer spectroscopy (CEMS), conversion x-ray Mössbauer spectroscopy (CXMS) and x-ray diffraction (XRD) have been used at CSM to identify the surface phases before, during and after the wear tests. These techniques have been described in some detail [2]. The study showed that the wear resistance is determined by which nitride is formed; ranked from most to least wear resistance, these are γ'-Fe_4N, ϵ-Fe_3N, and ζ-Fe_2N. There was no evidence of long range nitrogen migration occurring during the wear tests, often speculated to occur by others. This thesis describes studies of nitrogen implanted 304 SS and 310 SS.

The purpose of this study is to investigate the surface microstructure of a series of 304 SS and 310 SS samples with various nitrogen implantation doses at various implantation temperatures and dose rates. The techniques of CEMS, CXMS and XRD will be used and the results will be correlated with the modification of sliding wear behavior in order to establish the mechanisms responsible for the implantation induced improvement. We will also attempt to form thick

nitride layers with high implantation doses and to determine the optimum implantation temperatures, in order to produce more durable materials.

Austenitic stainless steel 304 and 310 have been chosen for this project because they are part of a family of alloys with a common face-centered-cubic crystal structure (fcc). We will compare their behavior with that of the simple microstructure of pure iron which is body-centered-cubic (bcc). Another reason for choosing the steels is that austenitic stainless steels are very widely used materials. They have outstanding corrosion resistances over a wide range of temperatures. They do not become brittle at sub-zero temperatures even as low as -240°C [4]. Unfortunately, they are rather soft materials and therefore often have poor wear resistance. Surface modifications might extend their use in tribological applications.

2. LITERATURE REVIEW

Recently, several groups have studied various stainless steels. It is well known that the austenitic stainless steels based on the Fe-Cr-Ni system have poor wear characteristics during sliding contact. The reason for this poor wear behavior is not well understood [5].

A recent survey [6] has provided useful relative wear data for a variety of stainless steels, but explanations for the observed range of responses have not been given. The work of Yang et al. [7] has shown that the debris particles from self-mated unimplanted 304 SS are strongly ferromagnetic and that those from 310 SS are non-magnetic. The debris particle size increased with higher sliding speeds, i. e. higher surface temperature. This verified the importance of the formation during wear testing of strain-induced martensite (body-center-tetragonal, bct) in some stainless steels. Their wear tests showed that 304 SS had the worst wear resistance and 310 had the best wear resistance and that the wear resistance depends on the stability of the austenite phase.

Several previous studies [7-9] on unimplanted samples found that martensite is formed not only during wear testing, where formation of martensite is expected due to large strains, but also during polishing prior to wear testing.

The results of the work by Spalvins [10] showed that ion-nitriding is a beneficial surface treatment for austenitic stainless steel. This is because austenitic stainless steels contain strong nitride-forming

elements such as Cr. In the ion-nitriding process, impinging ions deliver enough energy to the specimen, which is the cathode of a d.c. glow discharge, to heat it to a preselected nitriding temperature. Usually, the nitriding temperature ranges from 490 to 565°C. This diffusion-based process forms complex nitrides with a distinct compound layer. The compound layer increases surface hardness and thus improves wear resistance. Many kinds of stainless steels such as AISI-304, 305, 310, and 316 etc. have been examined [10]. It was found that the 304 SS which is the least stable with respect to the austenitic-martensite phase transformation exhibits a great improvement of the surface properties after ion-nitriding.

Much work has been done on ion implanted 304 SS by different groups. The work of Daniels and Wilbur(at CSU) [11] showed that nitrogen implantation of 304 SS (with an ion energy of 60 keV, a current density of 100 $\mu A/cm^2$ and a nitrogen ion dose of 2 X 10^{17} N^+_2/cm^2) induces an increase in the load-bearing capacity to over 40 times that of unimplanted 304 SS.

Oliver's group [12] has shown that the friction coefficient of 304 SS was not changed significantly by nitrogen implantation (with an energy of 90 keV, a current density of 5 μA/cm2, and a dose of 3.5 X 10^{17} ions/cm^2) and the initial wear rate for the implanted 304 SS was at least 20 times slower than unimplanted 304 SS. No evidence of a distinct two-stage wear process was found. Suri et al. [13] found that nitrogen implantation of 304 SS (with a nitrogen concentration of 10^{17} ions cm^{-2}

and at 50 keV) increases the wear rate initially, but that the wear rate approaches that of unimplanted 304 SS when the sliding distance increases up to 1000 m. They said that the reason for the result they obtained could be an increase in surface temperature at the wear surface during the wear test, thereby causing the removal of the implanted ions near the surface by diffusion.

Singer's group [14] measured the friction and wear resistance of 304 SS implanted with a fluence of 4 X 10^{17} N/cm^2 at 180 keV, using a hardened steel ball sliding (speed = 0.1 mm/sec) against the implanted steel. The results showed that nitrogen implantation did not reduce friction but delayed wear by increasing the resistance of the surface to shear. No significant nitrogen migration was found to occur during the wear test. Also they found that nitrogen implantation decreased the abrasive wear resistance due to a decrease in the ductility of 304 SS. They suggested that the reason for decreasing the ductility of 304 SS is that nitrogen implantation produces defect clusters and small dislocation loops in metals. This is in agreement with Moore et al. [15] who found that soft pure metals may have a high abrasive wear resistance because of their higher ductility. It has been also suggested [16] that nitrogen implantation decreases the abrasive wear resistance because of a transformation of the surface martensite to austenite. They also point out that temperature increases (to 500°C) during implantation could be the major factor to cause the martensite to transform. Those samples were polished and implanted with nitrogen with a dose of 2 X 10^{17} ions

/cm^2 using ion energies of 40 keV and 75 keV. The temperature used was 200°C. The abrasive wear was determined by using 3 μm diamond particles. The recent results of Singer at al. [17] with N, Ni, and Ne ion implantation suggest that the presence or absence of martensite in the 304 SS surface before wear testing is not a major factor in decreasing the wear resistance. Another important aspect of this study [17] was the study of implantation-induced phase formations. They suggested that the phases formed depend on the starting microstructure.

Shrivastava et al. [18] showed an increase of the surface hardness of 304 SS after annealing (from 120°C to 520°C) samples implanted with 5 X 10^{16} ions/cm^2 at 130 keV. They suggested that annealing reduces the dislocation density and this releases N which then goes into solid solution and increases the yield stress and therefore the hardness.

It is known that martensite will form in austenitic 304 SS when it is deformed. Work by Wagner et al. [9] and Vardiman et al. [16, 19] has shown that nitrogen ion implantation causes a transformation of the martensite to austenite; however, with increasing implantation dosages a reverse transformation occurred, from austenite to martensite. This behavior is surprising because of the stabilizing effect of N. A possible explanation could be the formation of Cr-nitrides which destabilize the austenite. Also, high implantation temperatures decreased the N content of the Fe-nitrides and increased the formation of Cr-nitrides.

The studies of phase transformations of a N implanted austenitic

stainless steel (Cr/Ni 18/9) by Leutenecker et al. [20] indicated contradictory results: transformation of martensite and austenite in both directions; higher N concentration causes N in solution and lower concentration causes nitride precipitation. The studies suggested that the treatment required to create a hard, thick ϵ-nitride layer on Fe-Cr-Ni steel is a temperature between 200°C to 300°C and a current density $\geq$ 40 $\mu A/cm^2$.

From our literature review, we found that N ion implantation of 304 SS and 310 SS generally improves the surface mechanical properties. The explanations are different. Some of them focused on the phase formation and some of them only focused on the surface properties. No reports have been found concerning the systematic study of surface tribological property improvement of N implantation before, during and after wear tests using Mössbauer techniques. From our pure iron study, we found that CEMS and CXMS techniques are useful techniques for identifying the phases. The amount of N bound to Fe and the thickness of the nitride layers can be determined from the fraction of the nitride phases measured by CEMS and CXMS. These Mössbauer techniques are ideal for the detection of martensite in stainless steel, which according to the literature is crucial to understand the wear behavior, especially for 304 SS.

3. EXPERIMENTAL TECHNIQUES

3.1 SAMPLE PREPARATION

Washer-shaped discs with an outer diameter of 4.6 cm, an inner diameter of 1.43 cm, and thickness 0.18 cm were machined from 304 SS and 310 SS alloy plates. The nominal compositions of 304 SS and 310 SS are listed in Table 1 [4].

TABLE 1. Composition of the Austenitic Stainless Steels

TYPE	Fe	C	Mn	P	S	Si	Cr	Ni
304(wt.%)	70.85	0.08	2.00	0.045	0.03	1.00	18.00	8.00
(at.%)	69.53	0.37	1.99	0.080	0.05	1.95	18.97	7.06
310(wt.%)	53.18	0.25	2.00	0.045	0.03	1.50	24.00	19.0
(at.%)	51.86	1.12	1.97	0.080	0.05	2.89	24.94	17.49

From Table 1. we see that the main differences in composition between 304 SS and 310 SS are their chromium and nickel contents. Greater Cr and Ni content results in higher temperature corrosion resistance [4], and also increased stability with respect to transformation to the martensite structure.

The surfaces of samples were ground flat and parallel, then one surface was polished with 6 μm diameter grit and fine polished with 0.3 μm alumina grit until a smooth surface relatively free of scratches was obtained. Prior to N implantation, each sample was cleaned ultrasonically

for 5 min in trichloroethylene in order to remove any oil or grease. This was followed by acetone and methanol cleaning before drying the samples with warm air.

3.2 NITROGEN IMPLANTATION

N implantation was done by our collaborators at CSU. The ion implanter at CSU (Fig. 1) is a unique instrument which is based on ion-thruster technology. It can operate at very high current densities (e.g. 1500 $\mu A/cm^2$) over a large area (from 3 cm to 10 cm in diameter). These features allow much shorter implantation times compared to conventional implanters. Gaseous ions such as nitrogen, oxygen, argon, and carbon have been successfully used in this system to implant many different metal surfaces. The ion source along with the discharge power supplies produces a uniform ion beam with a mixture of about 70% N^+_2 and 30% N^+ [21]. The ion beam current density can be adjusted from 10 to 1500 $\mu A/cm^2$ over an ion energy range from 10 to 80 keV. More details can be found in [22, 23].

For our study, samples were clamped to a fixture (sample holder) by a machine screw and implanted with nitrogen at an energy of 60 keV and a current density of 100 $\mu A/cm^2$ or 500 $\mu A/cm^2$. All the samples investigated are listed in Table 2 where samples are grouped according to total dose.

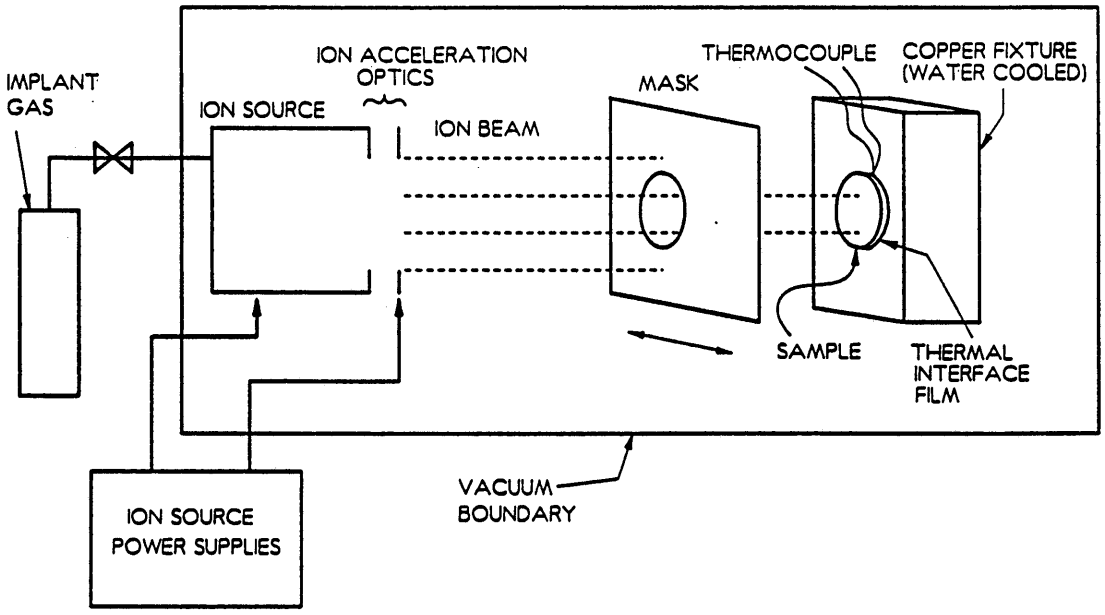

Fig. 1 Nitrogen Implanter

Eight 304 SS samples were implanted with different total dose at different temperature and four 310 SS samples were implanted with different total dose at the same temperature. Sample S0-2 was implanted with a dose rate of 500 $\mu A/cm^2$. The rest of them were implanted with a dose rate of 100 $\mu A/cm^2$. Usually, it is difficult to control the temperature during implantation due to variable thermal contact resistance between the samples and the sample holder through which water or liquid nitrogen is circulated. Here it was controlled by interrupting the beam periodically to keep the measured temperature within ± 50°C of a desired value. This was aided in most cases by using a thermal insulator (Kapton film) between sample and holder. No thermal contact medium was used for samples S1-1 and S3-1 and this metal-metal contact kept the temperature relatively low. One sample (S12-1) used a silver paint contact to produce the lowest temperature. Other samples, such as S1-1, and S7-1 were subjected to higher temperatures during implantation by using Kapton and no beam interruption.

The average range of implanted ions into 304 SS at the energy of 60 keV is about 650 Å for N^+, and at the energy of 30 keV is about 333 Å [24]. In our case, the implanted ions are a mixture of about 70% N^+_2 and 30% N^+ with the energy of 60 keV. When N^+_2 with the energy of 60 keV reaches the specimen, each N^+_2 will separate into two N^+ each with an energy of 30 keV. We estimate the mean range for this mixture of ions as:

TABLE 2. A List of Samples and Implantation Conditions

Sample No.	Total Dose (ions/cm^2)	Time at Temp. (min:sec)	Imp.Time (min:sec)	Temp. (°C)	Thermal Contact
S0-1[1]	0			0	---
S5-1	0			0	---
S1-1	$0.5X10^{17}$	1:20	1:20	280	M-M[2]
S7-1	$0.5X10^{17}$	1:20	1:20	400	M-M
S12-1	$1X10^{17}$	2:40	2:40	160	S-P[3]
S0-2[4]	$1X10^{17}$	6:00	2:40	340±50	M-M
S4-2	$1X10^{17}$	6:30	2:40	380±50	K[5]
S3-1	$4X10^{17}$	10:40	10:40	350	M-M
S9-1	$4X10^{17}$	40:30	10:40	380±50	K
S8-1	$10X10^{17}$	98:48	26:40	380±50	K
T0-2[6]	0			0	---
T1-1	0			0	---
T1-2	$0.5X10^{17}$	2:48	1:20	380±50	K
T0-1	$1X10^{17}$	9:24	2:40	380±50	K
T2-1	$4X10^{17}$	55:30	10:40	380±50	K
T3-1	$10X10^{17}$	129:54	26:40	380±50	K

1 S implies 304 SS
2 M-M implies metal-metal contact
3 S-P implies Silver Paint
4 Implanted with a dose rate of 500 μA/cm^2
5 K implies Kapton
6 T implies 310 SS

$$\langle R \rangle = 0.70 \times 333\ (Å) + 0.30 \times 650\ (Å) = 430\ (Å) \qquad (1)$$

This is consistent with the AES depth profiles (discussed later) from samples that are kept cool enough to prevent diffusion of N (≤200°C).

3.3 WEAR TESTING

Wear testing was done by the group at CSU by using a modified pin-on-disc wear tester. The concept by which the wear tester operated is illustrated in Fig. 2. As the figure suggests, the system produces a uniformly worn area on samples which are rotated at a speed of 80 rpm (1.3 Hz) under a lubricated condition. During the wear testing, a cylindrical pin with a diameter 6.4 mm and a hemispherical contact surface (3.2 mm radius of curvature) moves along the radius back and forth over the surface (4.4 cm o.d. and 2.1 cm i.d.) of the rotating sample at a frequency of 0.2 Hz. The hemispherical surface of the pin is formed using a special tool and then polished similarly. The pin is not implanted because the hemispherical surface of the pin will wear away very quickly to a depth beyond the N-implanted layer thickness [3]. A lubricant (10% oleic acid in kerosene) is supplied during the wear testing. Wear debris is collected with a filtering system in the circulating lubricant system. Wear is monitored by careful mass loss measurements. The tests on implanted specimens were conducted by increasing the load from 0.1 N until a sudden increase in sample mass loss was measured.

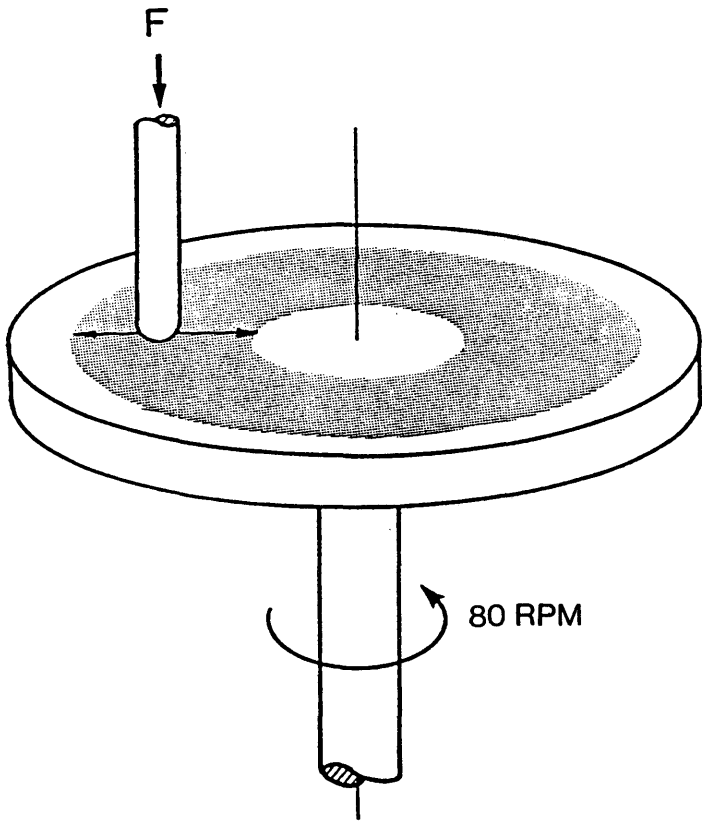

Fig. 2 Pin-on-disc Wear Tester

The corresponding load was designated the critical value for the sample. This method is different than that developed for N-implanted Fe in which the mass loss was monitored versus time at a constant load [3]. It was found that essentially no wear occurred versus time at a fixed load except for the unimplanted specimens.

3.4 MÖSSBAUER MEASUREMENTS

The Mössbauer effect is the phenomenon of recoilless resonance absorption of γ-rays. After the discovery by Rudolf Mössbauer in 1957, this method has been used in almost all areas of natural science because of the high energy sensitivity.

Narrow γ-ray energy distributions of about 10^{-9} eV (due to no recoil) allows the measurement of small perturbations of nuclear energy levels caused by the atomic environment of nuclei in solid materials. They are known as hyperfine interactions. The hyperfine parameters include the isomer shift (IS), the quadrupole splitting (QS), the internal magnetic field (H), and the line width (W). Many books and review papers describe the physics and applications of Mössbauer spectroscopy [25, 26].

For this research, the back-scatter Mössbauer methods, in particular ^{57}Fe conversion electron Mössbauer spectroscopy (CEMS) and conversion x-ray Mössbauer spectroscopy (CXMS), have facilitated the near-surface characterization of nitrogen-implanted 304 SS. In essence ^{57}Fe CEMS involves the detection of back-scattered electrons, mainly 7.3 keV

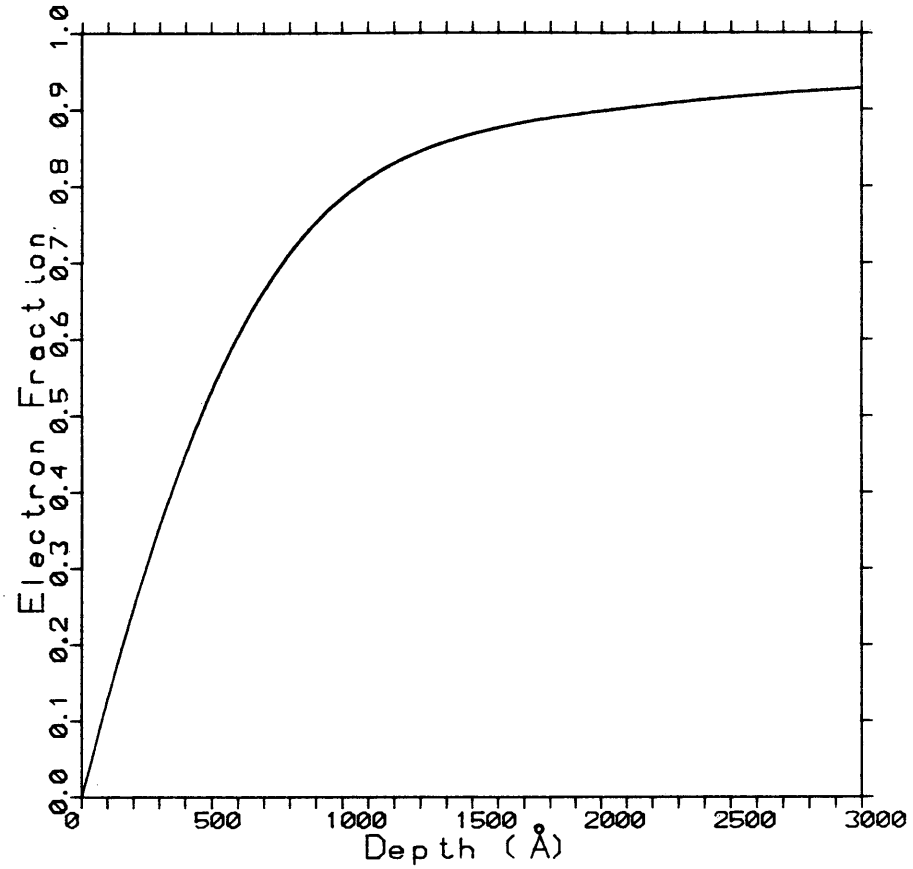

Fig. 3. The fraction of detected electrons corresponding to Mössbauer events which occur at depths D or less for 304 SS, 310 SS, and pure iron. (The three curves are not distinguishable due to very similar mass densities.)

K-shell internal conversion electrons, which are emitted with a 90% probability during the decay of ^{57}Fe subsequent to resonant absorption of γ-rays. CXMS involves detection of internal conversion x-rays that are produced with a 24% probability in the same process [26].

Fig. 3 and Fig. 4 show the probing depths of CEMS and CXMS for 304 SS and 310 SS compared to that of pure Fe. The theories used to produce these plots are discussed in [27]. As Fig. 3 suggests, pure Fe, 304 SS and 310 SS have almost the same electron fraction detected from a given depth. The theory [28, 29, 2] shows that the detected electron fraction from a certain depth of a given homogeneous sample is dependent only on the density of the material. Since the densities of pure Fe, 304 SS and 310 SS are 7.86, 7.90 and 7.93 g/cm^3 respectively, the curves are too close to distinguish. Fig. 4 shows that the detected x-ray fractions are different for the three materials at a certain depth. This is due to the fact [28, 29] that the mass absorption coefficients for the 6.40 keV x-ray are 534, 1078, and 1304 /cm for pure Fe, 304 SS and 310 SS, respectively. These linear absorption coefficients μ_a were calculated from:

$$\mu_a = q_a \Sigma_i W_i (\mu/q)_i \qquad (2)$$

where $(\mu/q)_i$ indicates the mass absorption coefficient (in cm^2/g) for the ith element of the alloy at the 6.4 keV x-ray energy, W_i is the weight fraction of the ith element in the alloy and q_a is the alloy mass density.

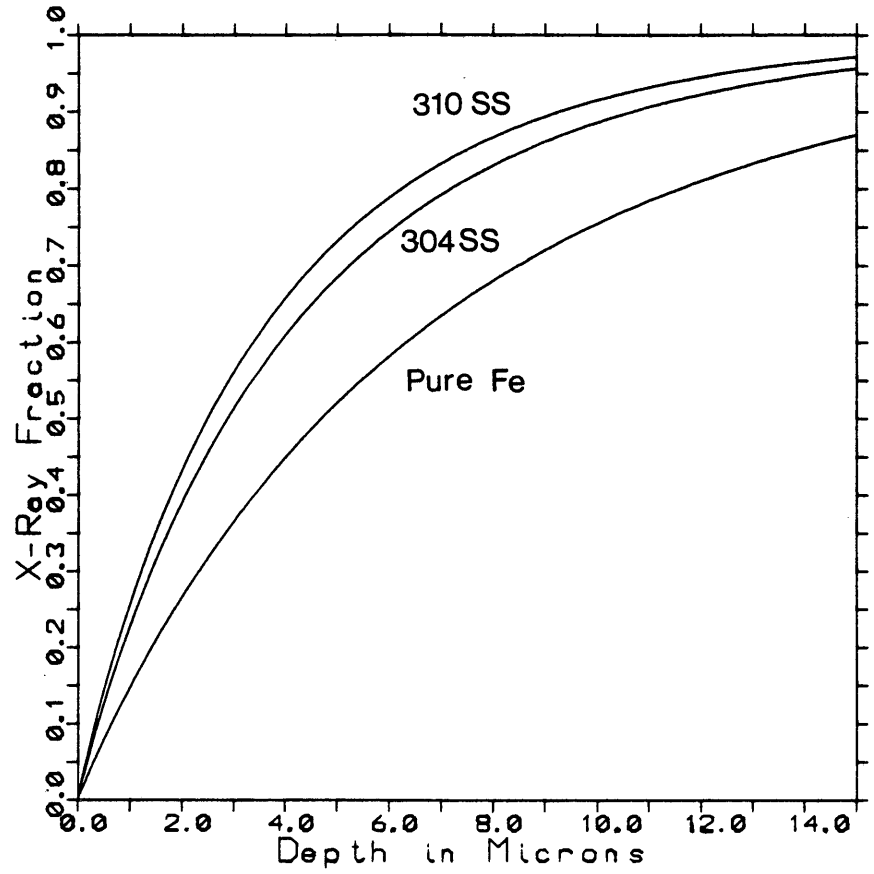

Fig. 4. The fraction of detected x-rays corresponding to Mössbauer events which occur at depth D or less for 304 SS, 310 SS, and pure iron.

There is a large increase in μ_a for the stainless steel compared to pure Fe due mainly to the absorption edge of Cr.

The radiation source consists of ^{57}Co doped into a rhodium foil. The excited state of ^{57}Fe, produced by electron capture in ^{57}Co, yields the 14.4 keV γ-ray upon deexcitation to the ground state. In the Mössbauer spectrometer the source is fixed on a driver rod. It oscillates with a constant acceleration which enables the energies of the emitted γ-ray to change linearly because of the Doppler effect and allows resonance between source and absorber over the range of velocity selected for the driver.

A gas-proportional counter was used as the CEMS and CXMS detector. He-(6.0%)CH_4 was used as the CEMS ionization gas and Ar-(10.0%)CH_4 was used as the CXMS ionization gas. In both cases, methane is a quenching gas to prevent a continuous electrical discharge in the counter. Details can be found in [27].

The spectra were fitted by using a program called Normos, which was provided by Dr. M. Kopcewicz of Warsaw University, Poland. Several changes have been made to the original program to allow the output of plot files and the parameters such as the absolute areas and the fractions of the phases. Because of the complex nature and incomplete resolution of the spectra from implanted samples, some of the fitting parameters were constrained in order to obtain consistent and physically reasonable results. In the fitting, the line width of the austenite (γ) phase was fixed at 0.3 mm/s, the FeN paramagnetic phase

line width was fixed at 0.5 mm/s, and the FeN magnetic stage was fixed at 0.6 to 0.7 mm/s for most of the spectra, in order to get the best fits. The IS of the austenite phase was fixed at -0.108 mm/s for 304 SS and at -0.104 for 310 SS, based on results from unimplanted specimens. For the six line resonance of magnetic phases, the ratios of the line width of 1 to 3 (W_{13}), and of 2 to 3 (W_{23}) were fixed at 3.1 and 2.4, respectively, for both CEMS and CXMS studies. The ratios of the intensities of 1 to 3 (I_{13}), and 2 to 3 (I_{23}) were fixed at 0.97, 1.24 for the CEMS studies and 0.92, 0.83 for the CXMS studies. These ratios were obtained by adjusting the parameters from fits of the magnetic martensite spectrum of wear debris from unimplanted 304 SS. These adjustments are consistent with the theory of the ratios of the area (width X intensity) of lines 1, 2, 3 (= 6, 5, 4) for magnetic phases, which are usually approximately 3:4:1 and 3:2:1 for CEMS and CXMS, respectively.

For some samples, nitrogen in solution was formed after nitrogen implantation. The fit of this expanded austenite phase with nitrogen in the solution was not fitted with a simple Lorentzian shape. Therefore, two doublets were used. One doublet was situated at -0.108 mm/s with a quadrupole splitting 0.15(2) mm/s using a fixed width of 0.3 mm/s. This doublet is attributed to the iron atoms which have no interstitial N as first nearest neighbors. Another doublet is at 0.20(3) mm/s with an adjustable quadrupole splitting, and a fixed width of 0.5 mm/s which is due to the N in solution. This doublet is due to those iron atoms which

have one or more nitrogen nearest neighbors.

3.5 OTHER MEASUREMENT TECHNIQUES

In our research, several other measurement techniques were used to complement the Mössbauer analysis and the mechanical testing. X-ray diffraction was used to obtain crystallographic phase information. This is important for stainless steel since phases could be present that contain little or no Fe and therefore not be detected by the Mössbauer effect. Auger electron spectroscopy (AES) depth profiling provided implanted nitrogen concentrations as a function of depth. Microhardness measurements provided hardness information on the implanted layer as well as the bulk. The XRD was done at CSM, the AES by a commercial firm [30], and the microhardness measurements by the group at CSU.

4. EXPERIMENTAL RESULTS AND DISCUSSION

4.1 UNIMPLANTED SAMPLES

Prior to being implanted with nitrogen, the samples were polished as described in section 3.1. Fig. 5 shows the CEMS measurements of one sample of 304 SS and one of the 310 SS after polishing. The fcc austenite is paramagnetic at room temperature and appears as a broad single line. The magnetic martensite phase is clearly seen in the 304 SS sample as a six-line resonance pattern. Evidence of martensite formation has appeared in all 304 SS samples examined after polishing (S4-2, S5-1, and S9-1). This austenite to martensite transformation is due to a strain-induced effect [19]. The amount of martensite in each sample is different because the polishing procedure and the associated surface strain is difficult to repeat exactly. The parameters of martensite(α') and austenite(γ) are listed in Table 3.

TABLE 3 CEMS Parameters of Polished, Unimplanted Samples

Sample No.	Phase	IS (mm/s)	QS (mm/s)	W_{34} (mm/s)	H (T)	F (%)	D (Å)
S4-2	α'	-0.01 (2)	0(f)	0.41(6)	26.3(7)	15(3)	144
	γ	-0.111(1)	0.15(1)	0.28(1)		85(1)	
S6-1	α'	0.02 (1)	0(f)	0.46(3)	25.3(2)	44(3)	383
	γ	-0.109(1)	0.16(1)	0.28(1)		56(1)	
S9-1	α'	-0.01 (f)	0(f)	0.50(9)	26.4(6)	14(2)	109
	γ	-0.108(1)	0.16(1)	0.28(1)		86(1)	
T0-1	γ	-0.104(f)	0.17(1)	0.29(1)		100	

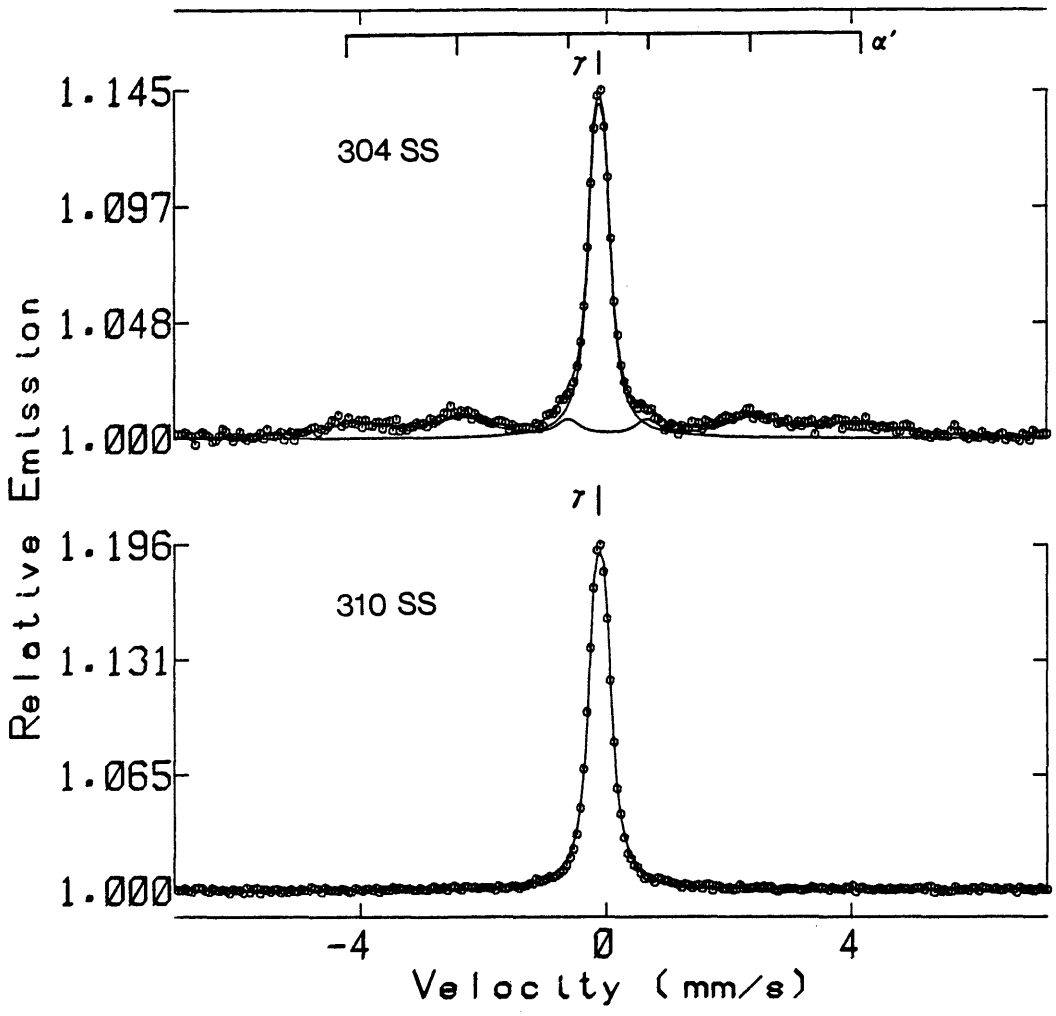

Fig. 5 CEMS Data of Polished 304 SS and 310 SS

F indicates the CEMS resonance fraction of the phase. W_{34} indicates the line width of the doublet or the two inner line widths of the six-line spectrum. f in parentheses means the parameter is fixed. The CXMS studies did not show the martensite phase on the polished samples. From this, it can be concluded that the martensite is formed as a near-surface layer. D in Table 3 indicates the estimated thickness of the martensite layer as obtained from the curve in Fig. 3 assuming the martensite is an uniform layer from the surface to depth D. The value of H $\approx$ 26 (T) is consistent with the known effect of Cr and Ni on H in ferrous alloys [31-33]. α' martensite did not form in 310 SS upon polishing because it contains more Ni, which stabilizes the austenite phase.

The broad paramagnetic resonance from austenite was fitted with a quadrupole pair which gives a much better fit than a broad single line. The origin of this broadening lies in the many near-neighbor environments of Fe atoms in the fcc alloy [34]. The random distribution of Cr, Ni and Fe neighbors produces distributions of quadrupole splittings and isomer shifts such that the fitted IS of -0.11 mm/s and a QS of 0.16 mm/s represent average values of such distributions.

Wear testing was then done on the unimplanted samples for a period of 25 hours with a load of 100 g using a pin of the same material as the disc. The Mössbauer results, shown (Fig. 6) that a large fraction of martensite was formed in 304 SS. The CEMS and CXMS data of sample S0-1 show that more martensite exists deeper than near-surface.

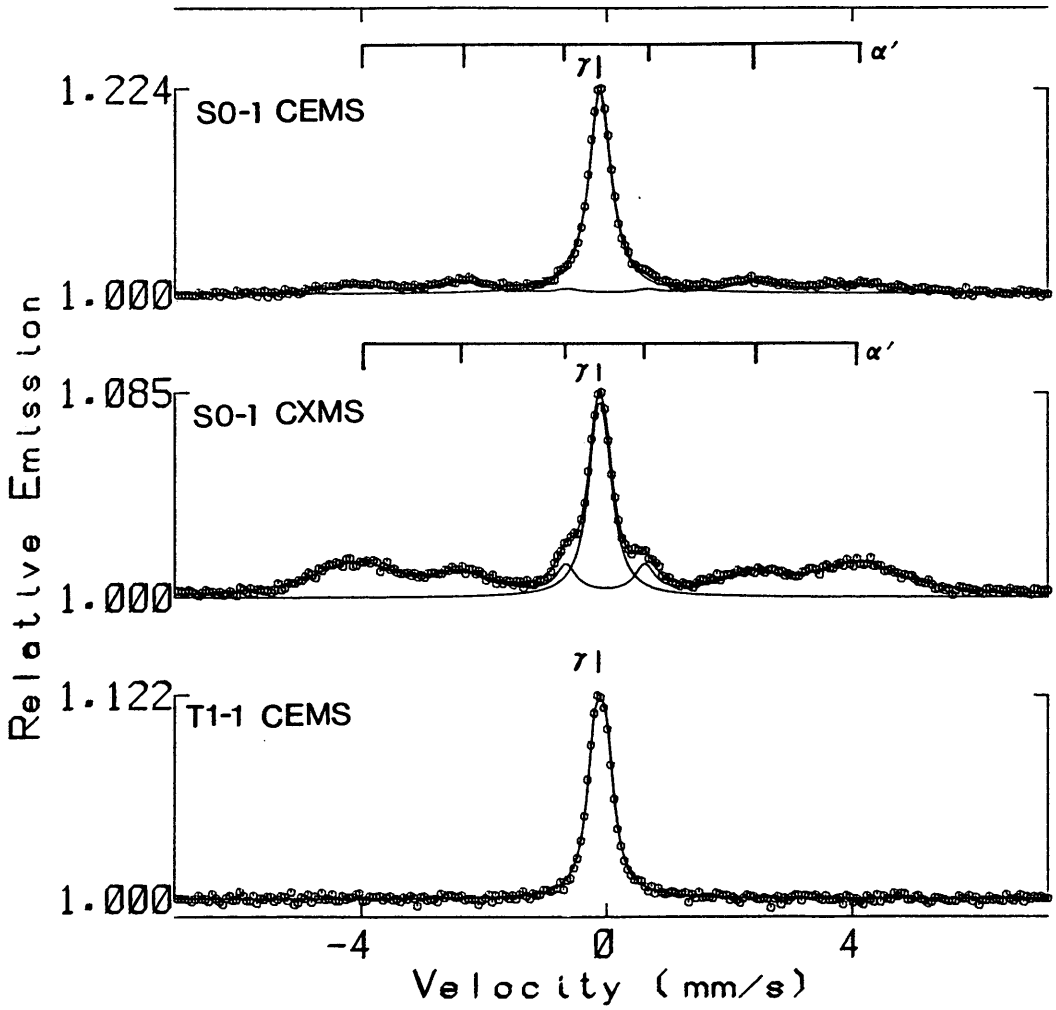

Fig.6 CEMS and CXMS of Unimplanted 304 SS and 310 SS after 25 h Wear

The results agree with the theory of the stress distribution at and below the contact areas of two solid bodies [19].

There was no martensite formed in T1-1. Thus, even for the severe stress associated with the wear test, the austenite remained stable. The CEMS and CXMS parameters are shown in Table 4.

TABLE 4 CEMS and CXMS Parameters of Unimplanted Samples after 25 Hours Wear

Sample No.	Phase	IS (mm/s)	QS (mm/s)	W_{34} (mm/s)	H (T)	F (%)
S0-1	γ	-0.108(f)	0.17(1)	0.3 (f)		52(1)
	α'	-0.01 (1)	0(f)	0.53(1)	25.0(1)	48(3)
cxms	γ	-0.108(f)	0.17(1)	0.3 (f)		29(1)
	α'	-0.02 (1)	0(f)	0.50(1)	25.5(1)	71(3)
T1-1	γ	-0.102(2)	0.18(2)	0.31(1)		100

Transmission Mössbauer spectra for the wear debris are shown in Fig. 7 and the parameters are listed in Table 5. They show that the 304 SS debris is highly enriched in α'-martensite compared to either the CEMS or CXMS results from the worn surface. No α'-martensite was detected in the 310 SS debris which is consistent with no martensite near the surface as detected by CEMS. There is a small amount of FeO in the wear debris, but whether this originated during or after wear is not known.

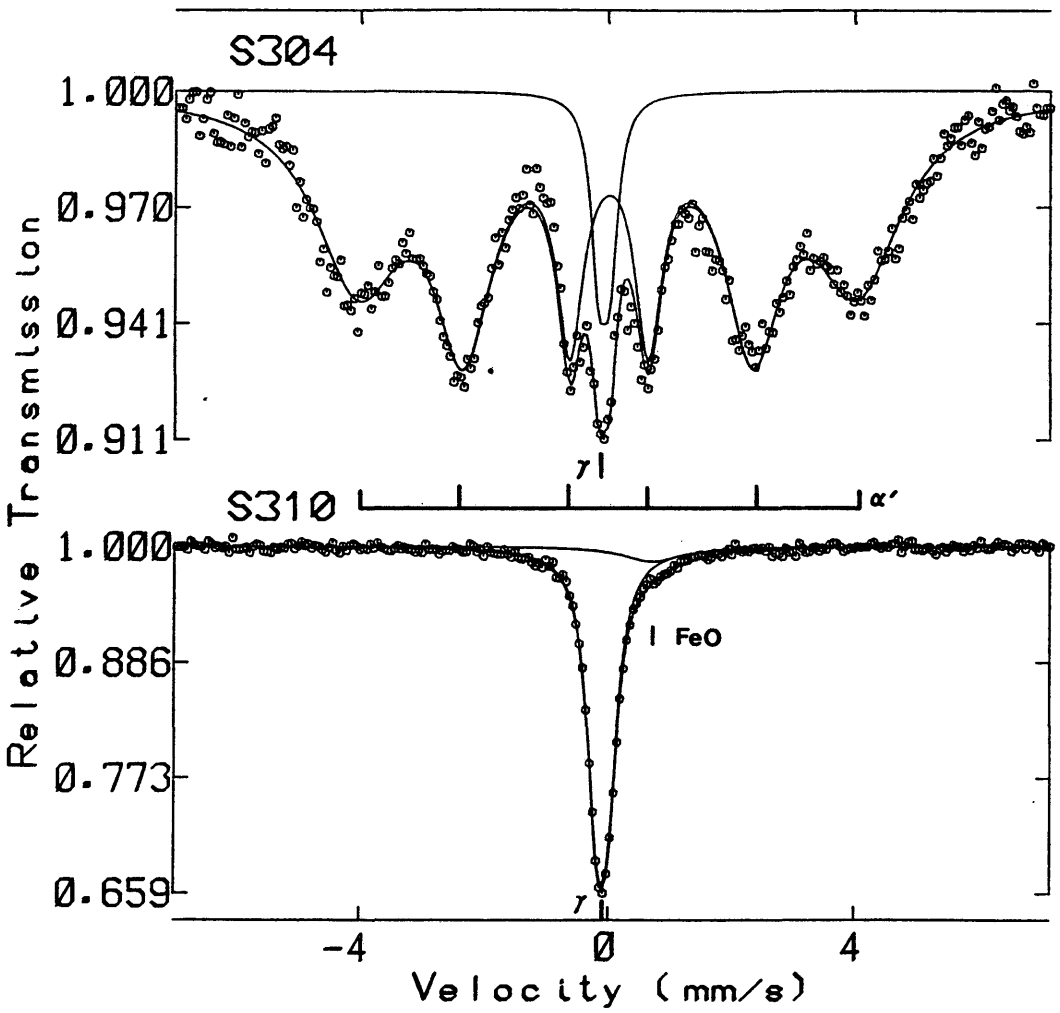

Fig. 7 Transmission studies for Wear Debris of 304 SS and 310 SS

TABLE 5 Transmission Mössbauer Parameters for Wear Debris of 304 SS and 310 SS

Sample No.	Phase	IS (mm/s)	QS (mm/s)	W_{34} (mm/s)	H (T)	F (%)
304SS	γ	-0.090(1)	0.19(1)	0.3 (f)		7(1)
	α'	-0.004(2)	0.01(1)	0.53(1)	25.16(1)	93(2)
310SS	γ	-0.104(f)	0.17(1)	0.36(1)		90(1)
	FeO	0.70 (f)		1.17(9)		10(1)

The phenomenon of strain-induced α' -martensite formation, which is clearly present in the 304 SS samples, is probably responsible for the difference in the sliding wear behavior of 304 SS and 310 SS. Fig. 8 shows that the metastable 304 SS has a higher wear rate than that of the stable 310 SS. Several researchers have found the same phenomenon [7-9], but no explanations have been given. We think one reason for this observation might be that the transformation from austenite to martensite in 304 SS causes a change in volume [35]. The lattice parameters of both Fe-C austenite and Fe-C martensite are known as a function of carbon content [36]:

$a_0 = 3.548 + 0.044\ x$ (Å) austenite-fcc

$a = 2.861 - 0.013\ x$ (Å) martensite-bct

$c = 2.861 + 0.116\ x$ (Å)

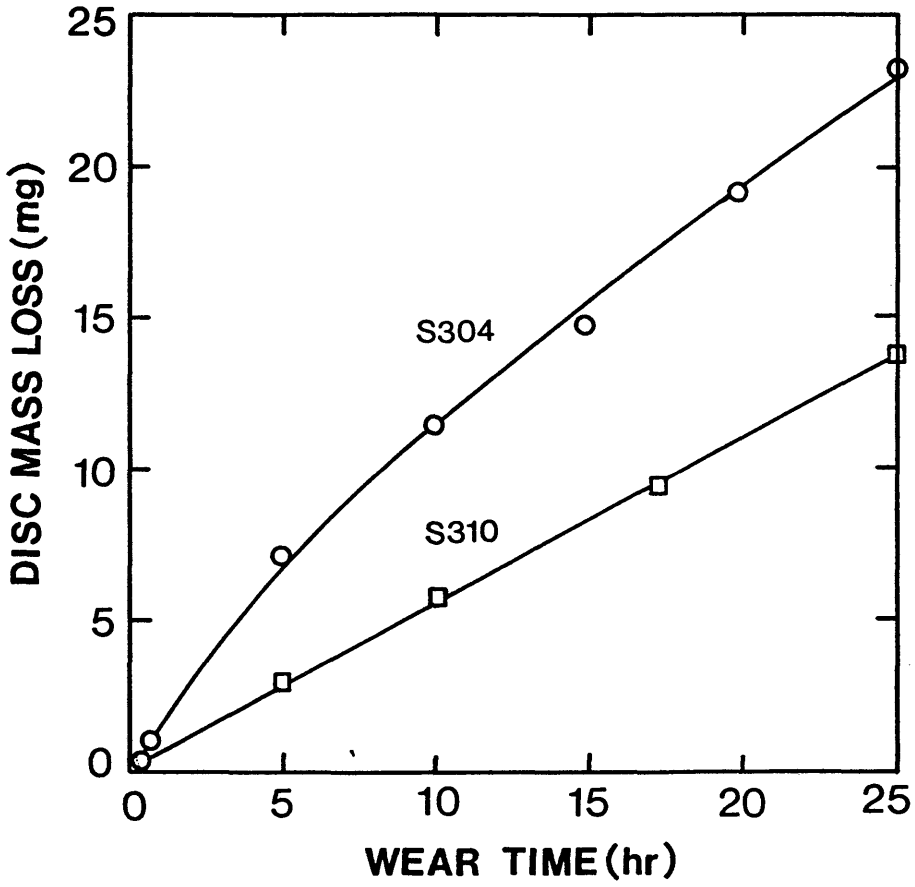

Fig. 8 Disc Mass Loss of 304 SS and 310 SS vs. Wear Time

where x represents the weight percentage of carbon. In 304 SS, x = 0.08(Table 1). So a_0 = 3.552 Å, a = 2.860 Å, c = 2.870 Å, and one finds the volume per Fe atom in austenite = $a_0^3/4$ = 11.20 Å and the volume per Fe atom in martensite = $a^2c/2$ = 11.74 Å. Therefore the transformation from austenite to martensite causes a volume increase of about 5 percent. This volumetric change produces high internal stresses which may generate microcracks in the steel. These cracks can propagate to the surface during the wear test and therefore lead to enhanced removal of martensite by the pin.

Some as-polished and unimplanted worn samples were also characterized by XRD. Results are listed in Table 6.

TABLE 6. X-ray Data for As-Polished Samples and Unimplanted 25 Hour Wear Test Sample

Sample	2θ	d(Å)	I	Phase
S4-2 (as-pol.)	43.3	2.08	100	γ
	44.2	2.05	7	α'
	50.4	1.80	32	γ
	74.5	1.27	30	γ
S5-1 (as-pol.)	43.3	2.08	100	γ
	44.2	2.05	8	α'
	50.3	1.81	30	γ
	74.5	1.27	10	γ
S0-1 (25 h)	43.3	2.08	100	γ
	44.2	2.05	48	α'
	50.3	1.81	25	γ
	64.4	1.44	3	α'
	74.5	1.27	12	γ
	81.9	1.17	8	α'

Table 6 shows that as-polished samples S4-2 and S5-1 have a small amount of martensite. A large amount of martensite was detected by

XRD on sample S0-1 after the 25 hour wear test. This is consistent with the CEMS and CXMS results on these same samples. The Cu-Ka x-rays (8.05 keV) probe a sample depth similar to the CXMS (6.4 keV) (Fig. 4).

4.2 AS-IMPLANTED 304 SS SAMPLES

The Mössbauer, XRD and AES results from the as-implanted samples (Table 2) will now be discussed in order of decreasing implantation dose. For each dose, the effect of temperature during implantation and time-at-temperature will be the primary variables considered.

4.2.1 $10X10^{17}$ ions/cm^2

The highest implanted dose was 10 X 10^{17} ions/cm^2 in sample S8-1 maintained at a temperature of 380±50°C. Visual inspection of the surface of the disc suggested non-uniformity so two areas, A and B, were examined. Region A was a mixture of two colors, metallic and brownish. Region B (180° from region A) was uniformly brownish. CEMS studies, shown in Fig.9, demonstrate clear differences in the two regions (designated by S8-1A and S8-1B). In order to fit these spectra and account for the N-induced modifications, the following restrictions were used in fitting the data (Table 7): the austenite IS, W and the α' W were fixed at the known unimplanted values. The results of W from S8-1A in Table 7 for the γ_N and FeNM were then fixed in order to fit the spectrum from S8-1B and obtain a good comparison. A large amount of bcc (α) or martensitic α' that is low in Cr, referred to as α', was obtained in region A and only a small amount in region B. This suggests that the metallic area of region A became hotter and led to phase decomposition such that Cr was depleted from either or both of the austenitic or martensitic 304 SS matrix.

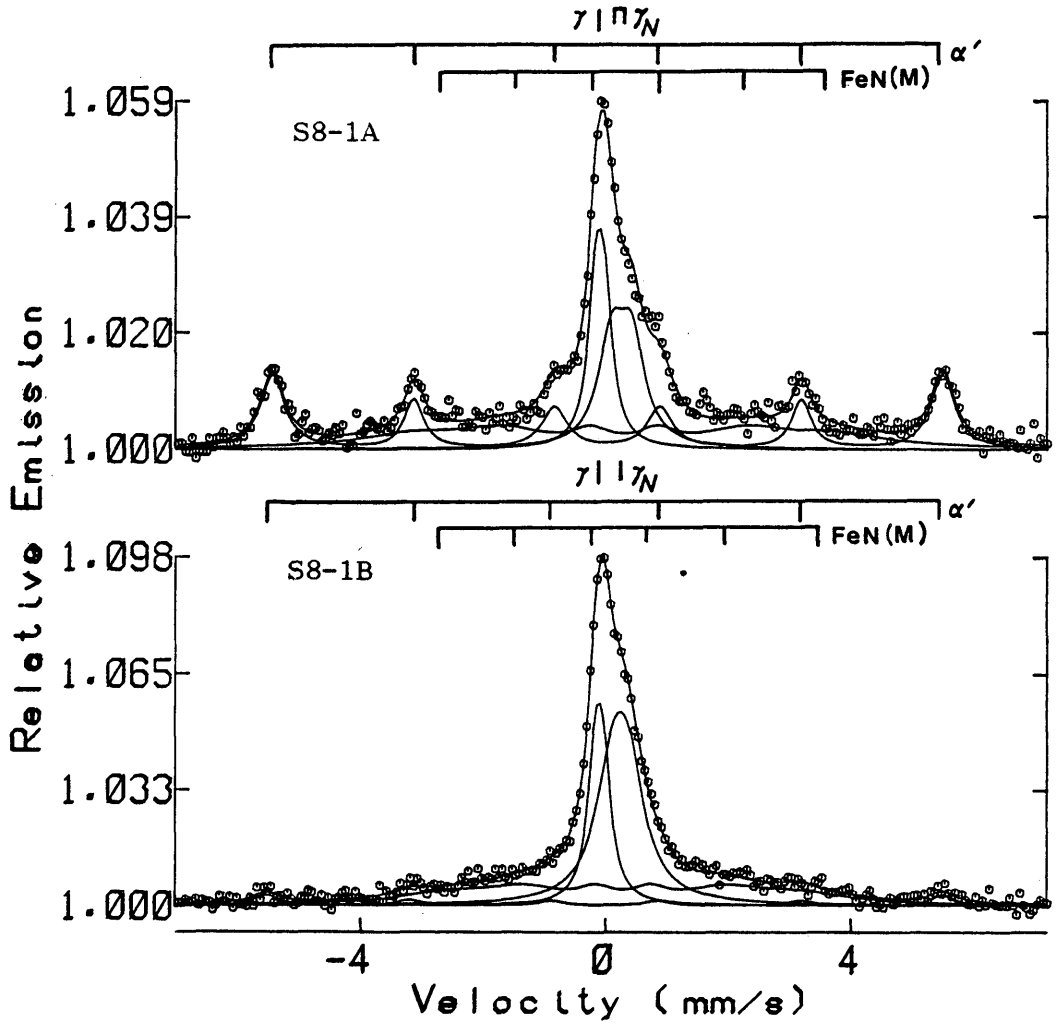

Fig. 9 CEMS Data of S8-1A and S8-1B

TABLE 7. CEMS PARAMETERS FOR S8-1A AND S8-1B

Sample No.	Phase	IS (mm/s)	QS (mm/s)	W_{34} (mm/s)	H (T)	F (%)	D (μm)
S8-1A	γ	-0.108(f)	0.15(1)	0.3(f)		17(1)	
	γ_N	0.24 (2)	0.32(3)	0.5(f)		22(1)	1.4
	FeNM	0.31(6)	0.00(f)	0.7(1)	21.2(6)	29(1)	.04
	α'	0.01(1)	0.00(f)	0.6(f)	33.7(1)	32(4)	
S8-1B	γ	-0.108(f)	0.14(1)	0.3(f)		23(1)	
	γ_N	0.26 (1)	0.28(1)	0.5(f)		33(1)	1.5
	FeNM	0.28(1)	0.00(f)	0.7(f)	17.1(7)	36(1)	.05
	α'	0.02(1)	0.00(f)	0.5(f)	33.9(2)	8(4)	

The effect of the N was to produce a paramagnetic resonance (designated by γ_N or FeNP) and a magnetic resonance (designated by FeNM) with a hyperfine field that is much smaller than that of α'. The smaller hyperfine field (17.1 T) for S8-1B is probably due to the higher concentration of Cr in solution in this region.

X-ray diffraction measurements from regions A and B are shown in Fig. 10. Diffraction peaks 2, 9 and peaks 1, 4, 7 are due to the aluminum sample holder used for S8-1A and S8-1B, respectively. Peaks 6 and 10 in S8-1A clearly indicate α' martensite. Peaks 5, 8, and 12 in S8-1A and 3, 6, 9 in S8-1B are due to the γ phase. By comparison with standard data, peak 5 (3 in S8-1B) was matched to phases with Miller indices γ(111), 8 (6 in S8-1B) to γ(200) and 12 (9 in S8-1B) to γ(220). Peaks 4, 7, 11 in S8-1A and 2, 5, 8 in S8-1B do not correspond to any nitride phase by comparison with standard data in the JCPDS File [37]. The fact that the three peaks appear just below the γ peaks suggests the possibility of a γ-phase with an expanded lattice constant. The lattice constant of SS is known [38] to increase linearly with N in solid solution. Therefore, peaks 4, 7, 11 in S8-1A and 2, 5, 8 in S8-1B are analyzed as the γ(110), γ(200), and γ(220) peaks of an expanded fcc phase designated as γ_N. CEMS studies on both regions show a clear ε-type phase which produces diffraction peak 3 in S8-1A and which produces a peak [FeNM] that is unresolved from peak 2 in S8-1B. The ε-type phase may affect the accurate determination of the positions of peak 4 in S8-1A and 2 in S8-1B.

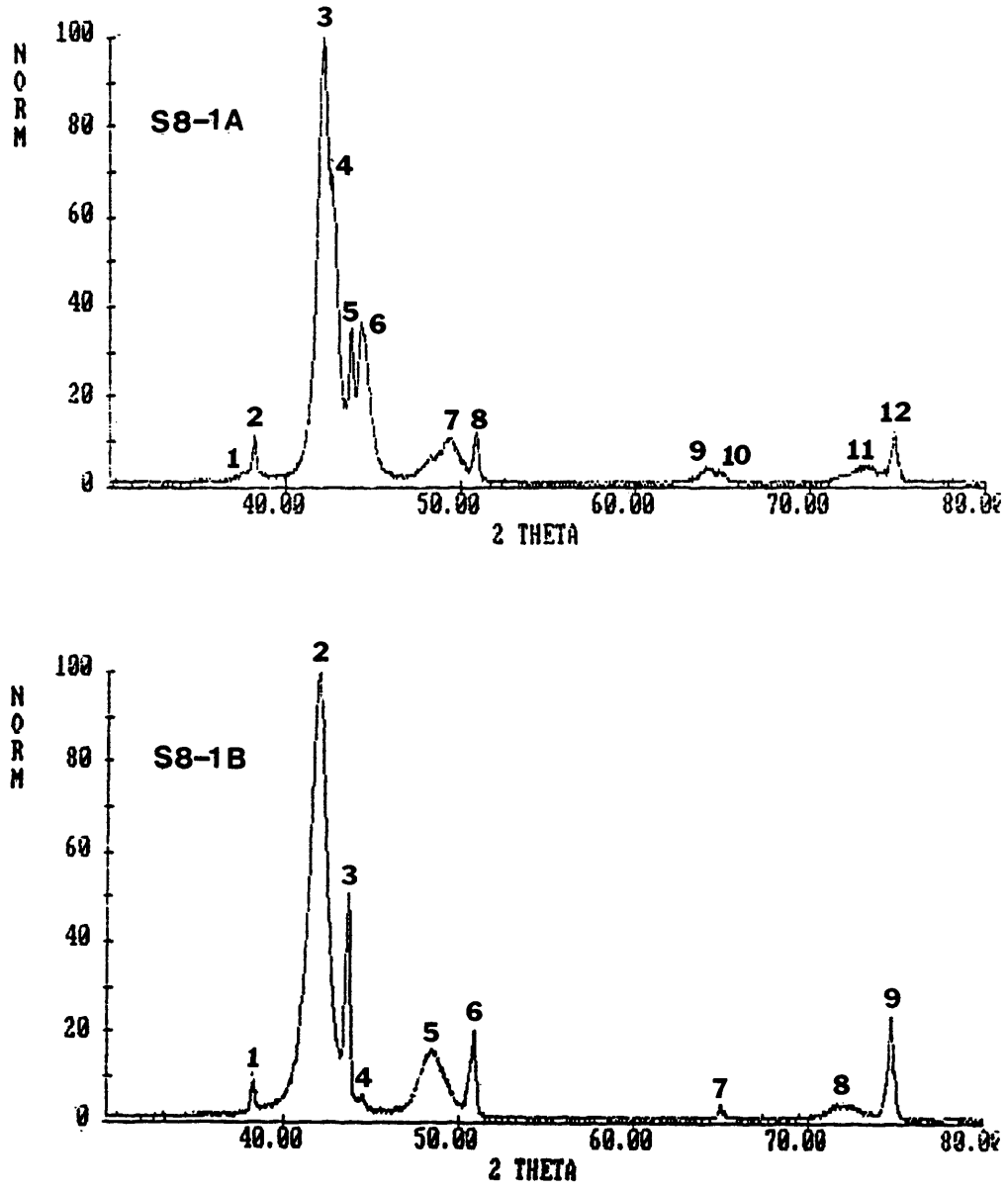

Fig. 10 XRD Data of S8-1A and S8-1B

TABLE 8 X-RAY DATA FOR IMPLANTED SAMPLE S8-1

Sample #	#	2θ	d(Å)	I	Phase	Δd/d
S8-1A	1	37.60	2.390	6.0	ε	
	2	38.26	2.351	11.7	Al(111)	
	3	42.22	2.140	100	ε	
	4	42.66	2.115	64.25	γ_N(111)	0.028
	5	43.76	2.067	36.6	γ(111)	
	6	44.34	2.041	31.1	α' (110)	
	7	49.35	1.845	11.7	γ_N(200)	0.029
	8	50.91	1.792	14.7	γ(200)	
	9	64.24	1.446	4.6	Al(220)	
	10	64.95	1.435	3.5	α' (200)	
	11	73.24	1.290	6.2	γ_N(220)	0.017
	12	74.82	1.268	12.2	γ(220)	
S8-1B	1	38.28	2.349	11.7	Al(111)	
	2	41.95	2.151	100	γ_N(111)+ε	0.039
	3	43.69	2.070	53.2	γ(111)	
	4	44.56	2.032	6.2	α' (110)	
	5	48.51	1.875	14.6	γ_N(200)	0.045
	6	50.85	1.794	22.8	γ(200)	
	7	64.90	1.436	3.5	Al(220)	
	8	71.91	1.314	4.3	γ_N(220)	0.035
	9	74.71	1.270	23.4	γ(220)	

Table 8 lists the x-ray data for S8-1. The fractional difference in d-spacing between the γ and γ_N phases, $\Delta d/d$, is also listed. It is suggested that the $\Delta d/d$ of the (220) peaks are smaller than that of the (111) and (200) for both regions because the larger angle corresponds to a deeper average probing depth where less nitrogen exists. A distribution in N content with depth is also suggested as the reason that the γ_N peaks are broad. These results are also consistent with CEMS studies, that higher temperature causes the nitrogen to diffuse deeper leaving less average nitrogen in solution in S8-1A than in S8-1B (less γ_N). The average nitrogen content in solution can be calculated from the average value of $\Delta d/d$ from the three peaks and the known [38] linear variation in lattice constant with atomic N content, C_N :

$$\langle \Delta d/d \rangle \, a_0 = 0.00078 \, \langle C_N \rangle \qquad (3)$$

a_0 is the lattice constant of 304 SS without N in solution and from the γ peak positions a_0 = 3.59 Å . For sample S8-1A, $\langle C_N \rangle$ = 11.3 at. %. and for S8-1B, $\langle C_N \rangle$ = 18.2 at.%.

The thickness of the layer containing the nitrogen in solution can be estimated by assuming it is a uniform layer from the surface to a depth z and using the areas (integrated intensity) of the (200) peaks [39]:

$$\frac{A(\gamma_N)}{A(\gamma_N) + A(\gamma)} = 1-\exp\left[-2\,\mu\,\frac{z}{\sin\theta}\right] \qquad (4)$$

$A(\gamma_N)$, $A(\gamma)$ are the areas of $\gamma_N(200)$ and $\gamma(200)$ peaks, respectively. μ is the absorption coefficient of the Cu K_α x-ray in 304 SS (2136 /cm) (or 310 SS (1830 /cm)) and θ is the average angle of the $\gamma_N(200)$ and $\gamma(200)$ peaks. This yields z = 1.4 μm and 1.5 μm for S8-1A and S8-1B, respectively. This is a very significant result since the mean implantation depth is only 430 Å as shown earlier (section 3.2). Clearly, diffusion of N occurs during the implantation process.

X-ray diffraction also shows that there is a well defined peak at about 2θ = 42.2 degree (d = 2.14) and a weak one at 37.6 degree (d = 2.39). The corresponding values of d are close to (111) and (110) planar spacings in a hexagonal ϵ-(Fe, Cr, Ni)$_{2+x}$N compound with x = 0 to 2 [37]. The (111) peak is the strongest one in the ϵ-(Fe, Cr, Ni)$_{2+x}$N powder pattern, and (110) should be 16% of this peak height. No other ϵ peaks could be detected in this sample. This suggests a strong preferred orientation of the (111) planes parallel to the surface of the disc. X-ray diffraction detected no CrN or Cr_2N in the sample. If present, as suggested by the Cr depleted martensite (α'), then they must be in the form of precipitates that are too small to be detected by XRD (≤100 Å).

The thickness of the ϵ-type phase layer was calculated from the theory used to generate the curves of Fig. 3 [27]. The assumption was made that the nitride phase is uniform from the surface to a depth D. The other two properties needed are the mass density and the atomic concentration of Fe in this phase. Assuming the phase is ϵ-(Fe, Cr,

$Ni)_2N$ with Fe, Cr, and Ni concentrations in direct proportion to those of 304SS (Table 1), then values of D = 390 Å and 450 Å are obtained for S8-1A and S8-1B, respectively. These values represent the maximum possible thickness of a uniform layer of the ϵ-type phase since the density and Fe concentration are minimum for this nitrogen content.

The AES profile for S8-1 is shown in Fig. 11. The nitrogen profile is non-gaussian with N distribution peak around 31 at.% near the surface. The sputter time for the sample is 85 min with a sputtering rate of 100 Å/min. Therefore the depth of the sputtering is 8500 Å. Clearly the N diffused very deep in the sample. This is consistent with our CEMS and XRD studies. Recall in section 3.2 that the mean range of the implanted N was found to be 430 Å so that the very broad N profile in Fig. 11 can only be explained by a diffusion mechanism. It can be mainly attributed to radiation enhanced diffusion since the ordinary thermal diffusion coefficient (D_T) of N in stainless steel [40]

$$D_T=0.06(cm^2/s)\exp[-21.7x10^3(K)/T] \qquad (5)$$

yields a diffusion length $\sqrt{D_T t}$ of only 106 Å using T = 653 K and t = 5928 s for sample S8-1 (Table 2). This suggests that the mechanism of radiation enhanced diffusion [41] must play an important role in the experimental N distribution. This may occur during the nitrogen implantation due to the production of vacancies which may allow nitrogen to diffuse more readily.

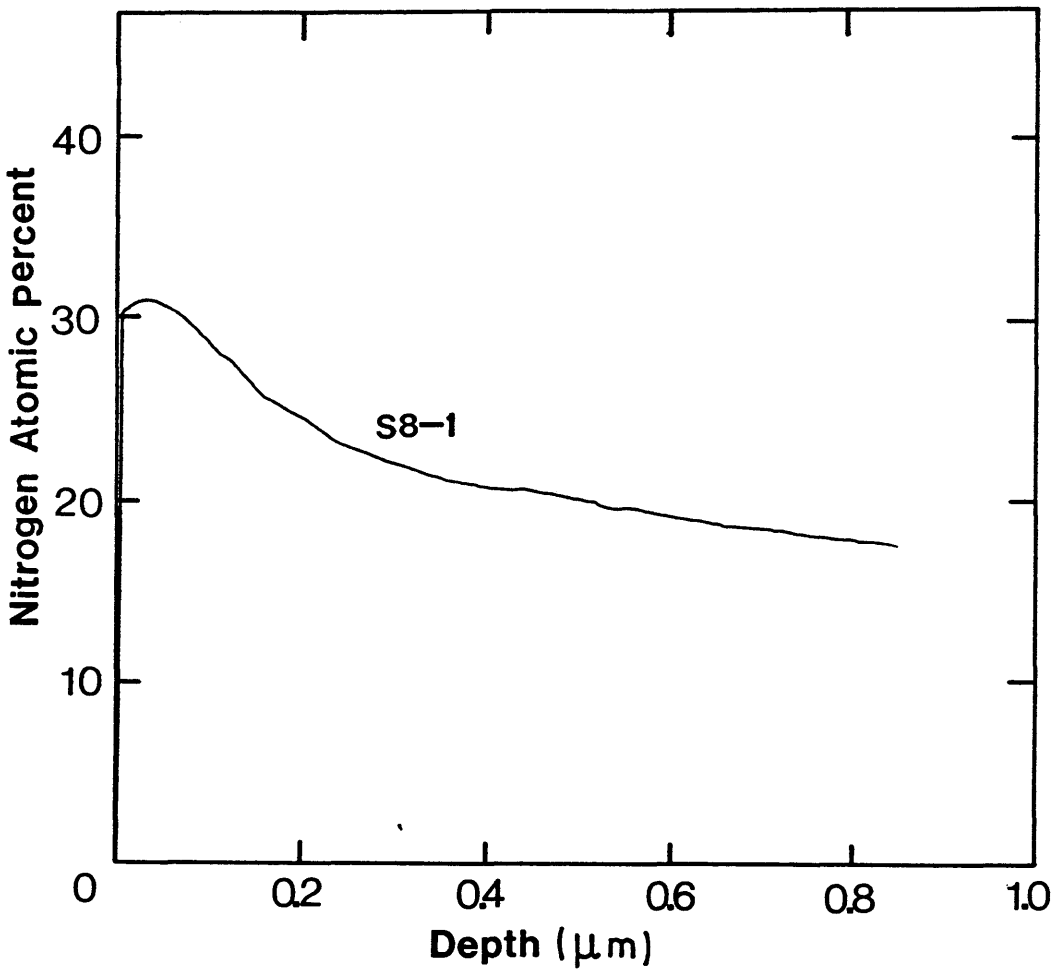

Fig. 11 AES Data of S8-1

4.2.2 $4X10^{17}$ ions/cm^2

Two samples, S3-1 and S9-1, were studied with this implantation fluence at different temperatures (Table 2). Note that sample S9-1 was held at the higher temperature for a longer time by using the shutter-control method. CEMS data are shown in Fig. 12. A paramagnetic nitrogen-containing phase and a magnetic nitrogen-containing phase are obtained in both samples after nitrogen implantation. It is obvious that sample S3-1 has a different paramagnetic phase (larger QS and IS) and a larger amount of the magnetic phase than S9-1. Table 9 lists the fit parameters for the phases identified in Fig. 12. The IS and QS for FeNP of S3-1 corresponds well to those of Fe_2N [42]. The FeNM parameters of S3-1 correspond to ϵ-(Fe, Cr, Ni)$_{2+x}$N with x = 1 to 2 similar to S8-1. Assuming an average of x = 1, the depth of the combined nitride phases in S3-1 is about D = 1300 Å based on the CEMS calibration (section 3.2). Bound nitrogen (B) can be estimated from the simple expression

$$B = qDN_a/W_a \qquad (6)$$

where q represents the average density of the nitride layer, W_a represents the average molecular weight and N_a is Avogadro's number. This gives B = 3.1 X 10^{17} N/cm^2, about a factor of two less than the implanted dose of 6.8 X 10^{17} ions/cm^2.

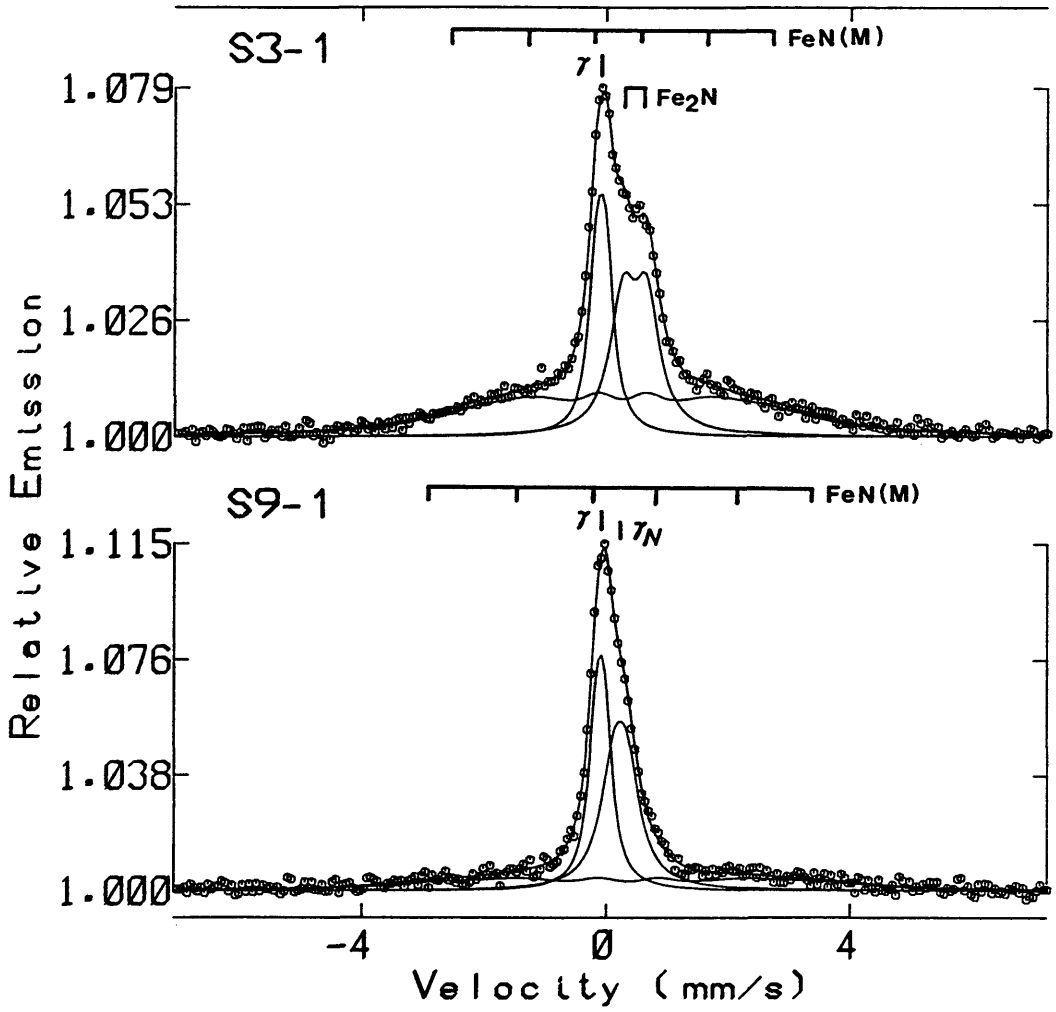

Fig. 12 CEMS of S3-1 and S9-1

TABLE 9 CEMS PARAMETERS FOR S3-1 AND S9-1

Sample No.	Phase	IS (mm/s)	QS (mm/s)	W_{34} (mm/s)	H (T)	F (%)	D (μm)
S3-1	γ	-0.108(f)	0.15(1)	0.3(f)		22(1)	
	Fe_2N	0.44 (1)	0.39(1)	0.5(f)		31(1)	
	FeNM	0.24 (2)	0.00(f)	0.71(6)	15.2	47(4)	.13
S9-1	γ	-0.108(F)	0.13(1)	0.3(f)		37(1)	
	γ_N	0.21 (1)	0.22(2)	0.5(f)		38(1)	0.6
	FeNM	0.32 (8)	0.00(f)	0.7(f)	18.9(9)	25(2)	.03

XRD of S3-1 shows a well defined peak at 2θ = 38.6° (d = 2.33 Å) and a broad peak at about 2θ = 41.2° (d = 2.19 Å) which are consistent with ϵ-(Fe, Cr, Ni)$_{2+x}$N (x = 0 to 2) [37]. No other nitride peaks or shoulders were detected. The XRD pattern for S9-1 is shown in Fig. 13 and the x-ray analysis is given in Table 10 together with that for S3-1. Peaks 1, 4, and 7 are due to the aluminum sample holder used. Magnetic nitrides and paramagnetic nitrogen containing phases both contribute to peak 2. Peaks 3, 6, and 9 indicate the γ phase (bulk 304 SS) and peaks 2, 5, and 8 are due to an expanded γ phase caused by N in solution as discussed earlier for S8-1. The amount of nitrogen in solution is about 16 at% based on the average Δd/d in Table 10. The depth of the layer containing the nitrogen in solution is 0.6 μm based on equation (4). The CEMS fit parameters of the paramagnetic phase of S9-1 (Table 9) IS = 0.21 mm/s and QS = 0.22 mm/s are similar to those of the N in solution resonance identified in S8-1. The magnetic nitride phase detected by CEMS is associated with the well defined peak 2 in the XRD and is attributed to ϵ-(Fe, Cr, Ni)$_{2+x}$N . No other ϵ peaks were detected. This is similar to S8-1 in that the (111) planes are preferentially parallel to the surface. No CrN or Cr_2N were detected by XRD. The thickness of the ϵ nitride phase is approximately 300 Å based on the CEMS fraction.

The difference in hyperfine field in the samples (15.2 T in S3-1 and 19.5 T in S9-1) could due to either different N or Cr contents in the nitride phase. Both N and Cr will reduce H [32, 43].

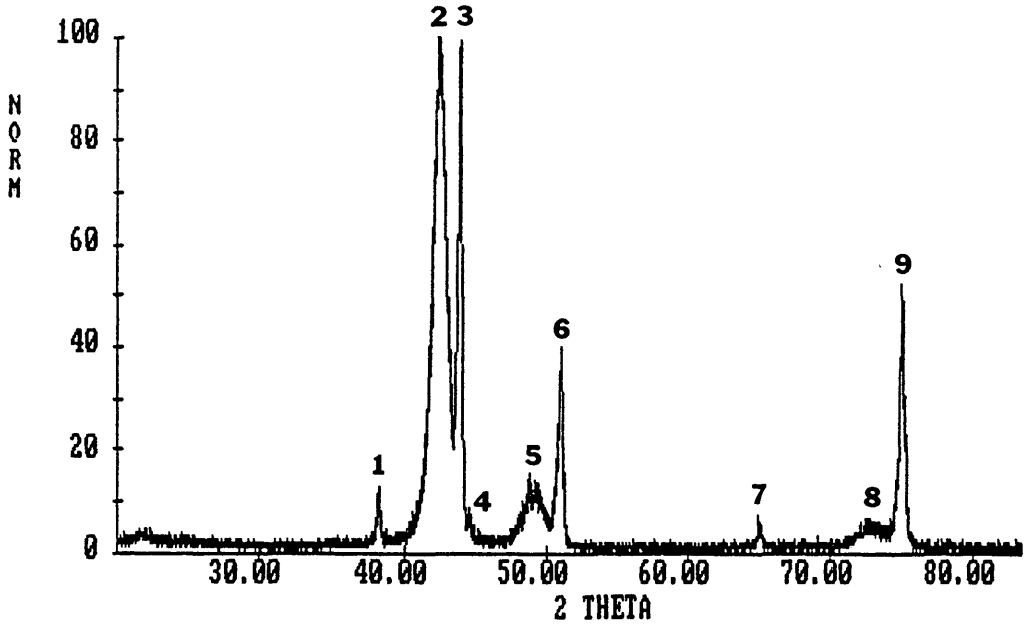

Fig. 13 XRD Data of S9-1

TABLE 10 X-RAY DATA FOR IMPLANTED SAMPLES S3-1 AND S9-1

Sample #	#	2θ	d(Å)	I	Phase	Δ d/d
S3-1	1	38.60	2.330	6.0	ϵ	
	2	41.20	2.189	3.0	Fe_2N	
	3	43.76	2.067	100	γ(111)	
	4	50.91	1.792	40.0	γ(200)	
	5	74.82	1.268	12.2	γ(220)	
S9-1	1	38.50	2.336	14.0	Al(111)	
	2	42.32	2.132	100	γ_N(111)+ϵ	0.030
	3	43.70	2.070	98.0	γ(111)	
	4	44.81	2.020	8.9	α' (110)	
	5	48.60	1.871	14.5	γ_N(200)	0.047
	6	51.05	1.787	39.4	γ(200)	
	7	64.80	1.437	6.3	Al(220)	
	8	72.30	1.305	6.2	γ_N(220)	0.030
	9	74.77	1.267	53.0	γ(220)	

The AES profiles for S3-1 and S9-1 are shown in Fig. 14. The nitrogen profiles are clearly non-gaussian. The peak of the N distribution of S3-1 is about 26 at% very near the surface and the width at half maximum is about 2400 Å. This value is nearly twice the depth obtained above from the CEMS nitride fractions, suggesting that the uniform layer assumption used for the determination of D is not correct. The total nitrogen remaining in the sample is about 4.2 X 10^{17} N/cm^2, estimated from the N profile. Note that this value does not agree with the bonded nitrogen estimated above. Thus, the retained nitrogen is not all in the form of nitrides. However, compared to the total implanted nitrogen (6.8 X 10^{17} N/cm^2, 70% N^+_2 + 30%N^+) some nitrogen was not retained. This loss of nitrogen is probably due to sputtering of the surface and to out-diffusion at the surface and possibly in-diffusion such that N is lost to the bulk. The thermal diffusion length is only 16 Å using T = 621 K and t = 640 s for S3-1 (Table 2) based on equation 5. Therefore, radiation enhanced diffusion also plays an important role in S3-1. Fig. 14 shows that the peak of the N distribution for S9-1 is about 31 at% and N-containing layer extended to a depth of about 0.6 μm in good agreement with the thickness of the N in solution layer calculated above from XRD data. The total nitrogen remaining in S9-1 is about 8.4 X 10^{17} N/cm^2. This value is higher than the implanted nitrogen (6.8 X 10^{17} N/cm^2). A possible explanation for the difference is that the AES calibration in thickness or atomic concentration is incorrect. In this sample, the

diffusion length is only 73 Å.

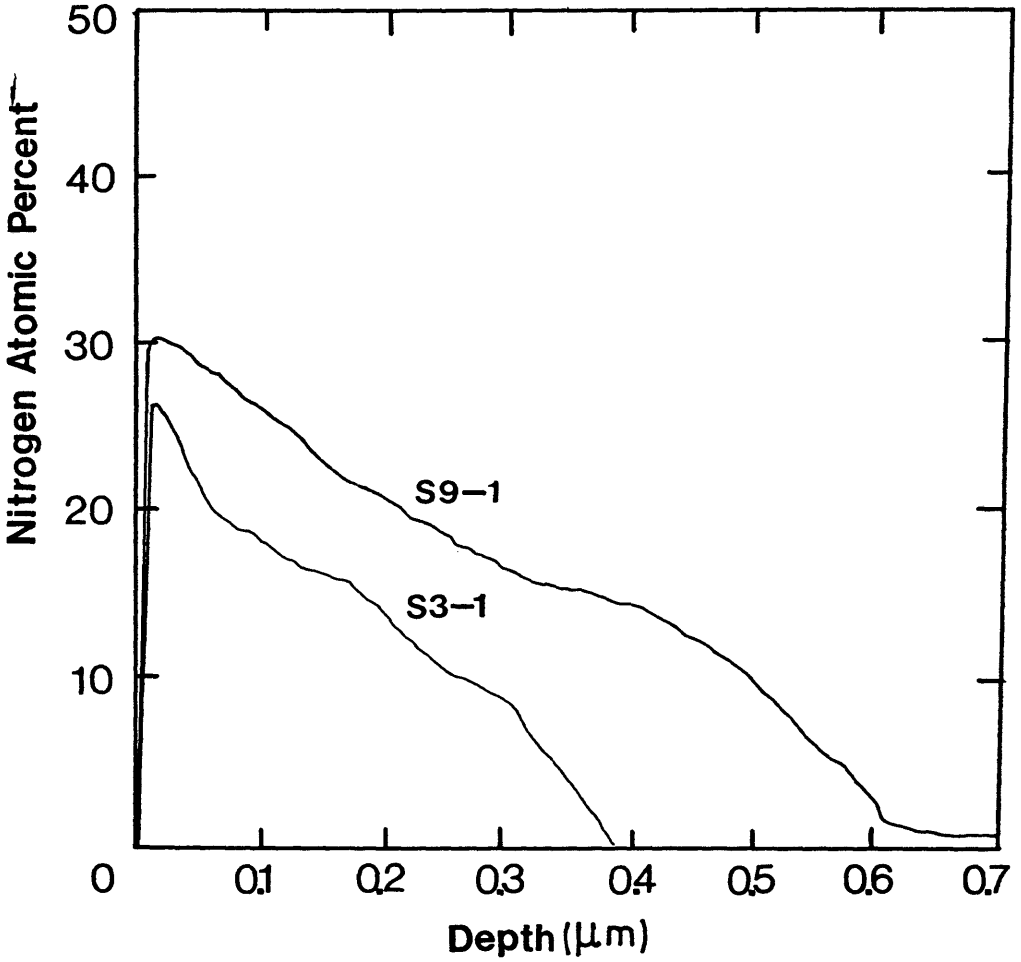

Fig. 14 AES Data of S3-1 and S9-1

4.2.3 $1X10^{17}$ ions/cm^2

Samples S12-1, S0-2, and S4-2 will be discussed in order of increasing implantation temperature. Sample S12-1 was implanted at the lowest temperature (T = 160°C) by insuring good thermal contact between the disc and the water-cooled sample holder. Fig. 15 shows that both a paramagnetic nitrogen-containing phase and a magnetic nitride formed in this sample. The fit parameters for S12-1 are listed in Table 12. The IS (0.36 mm/s) and QS (0.42 mm/s) of the paramagnetic nitride phase in S12-1 suggests that the nitride phase is ϵ-(Fe, Cr, Ni)$_2$N since ϵ-Fe$_2$N has similar values [44]. The magnetic nitride phase (FeNM) is very likely ϵ-(Fe, Cr, Ni)$_{2+x}$N with x = 1 to 2 similar to S8-1, S3-1 and S9-1, since ϵ-Fe$_3$N and γ'-Fe$_4$N are known to be magnetic [45, 46]. The small hyperfine field of 13.2 T is due to the presence of Cr in the nitride. The thickness of a combined layer of ϵ-(Fe, Cr, Ni)$_2$N and ϵ-(Fe, Cr, Ni)$_{2+x}$N is found to be D=730 Å, based on the assumption of a uniform layer (Fig. 3). The bound nitrogen (1.7 X 10^{17} N/cm^2 based on equation 6) agrees very well with the implanted dose of 1.7 X 10^{17} N/cm^2 suggesting that loss of N by sputtering or diffusion does not occur for this dose and temperature.

CEMS studies of samples S0-2 and S4-2 are also shown in Fig. 15. Only a paramagnetic nitrogen-containing phase exists in the two samples after nitrogen implantation. The IS and QS, listed in Table 11, show that the paramagnetic nitride phase for the two samples is not ϵ-(Fe, Cr, Ni)$_2$N as it was in S12-1.

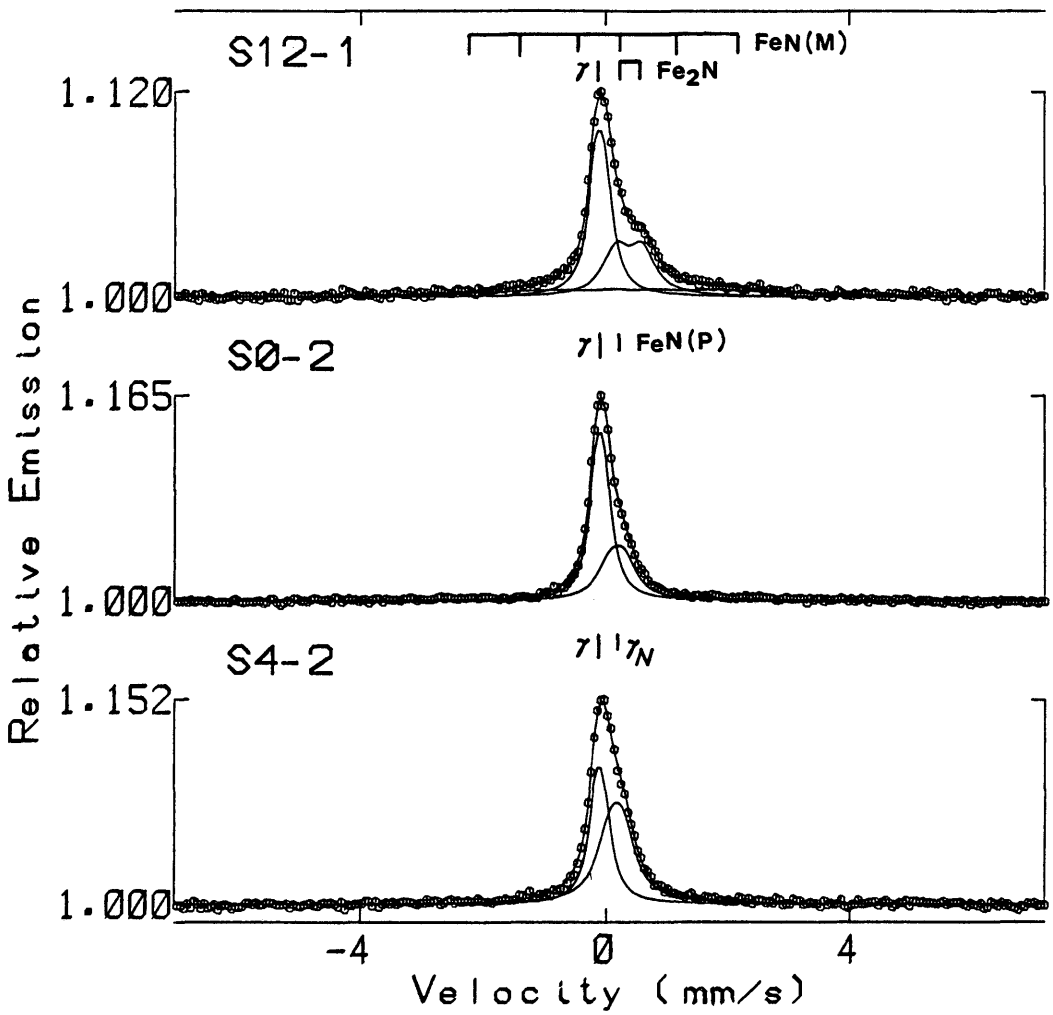

Fig. 15 CEMS Data of S12-1, S0-2, and S4-2

TABLE 11. CEMS PARAMETERS FOR S12-1,S0-2, AND S4-2

Sample No.	Phase	IS (mm/s)	QS (mm/s)	W_{34} (mm/s)	H (T)	F (%)	D (μm)
S12-1	γ	-0.108(f)	0.15(1)	0.3(f)		46(1)	
	Fe_2N	0.36 (1)	0.42(1)	0.5(f)		32(1)	
	FeNM	0.45 (2)	0.00(f)	0.7(2)	13.2(5)	23(5)	.07
S0-2	γ	-0.108(f)	0.14(1)	0.3(f)		44(1)	
	FeNP	0.18 (1)	0.23(1)	0.5(f)		36(1)	.05
S4-2	γ	-0.108(f)	0.13(1)	0.3(f)		44(1)	
	γ_N	0.15 (1)	0.22(2)	0.5(f)		56(2)	0.2

XRD studies (S12-1 and S4-2) are shown in Fig. 16, and the data are listed in Table 12. No Cr nitrides were detected by XRD for the three samples. Peaks 1 and 5 in S12-1 and 1, 4 and 7 in S4-2 are due to the aluminum sample holder. It is obvious that no N in solution (expanded γ phase) is shown in S12-1. This is consistent with our CEMS study which found ϵ-Fe_2N.

Peak 3 for S0-2 was due to the Al sample holder used. By comparison with standard XRD data, the paramagnetic nitride phase in S0-2 is more likely ϵ-$(Fe,Cr,Ni)_{2+x}N$ (non-magnetic) with x = 0 to 1 since the expanded γ phase is not detected by XRD. The thickness of this nitride of S0-2 is approximately 450 Å based on the CEMS fraction. The bound nitrogen (1.5 X 10^{17} N/cm^2 assuming D = 450 Å) used in equation 6 is close to the implanted one (1.7 X 10^{17} N/cm^2).

N in solution is obtained in S4-2 (peaks 5 and 8). The average content of nitrogen in solution is about 11 at%. The depth of the layer of the nitrogen in solution is about 0.2 μm based on equation 4 and using peaks 5 and 6. A uniform layer of 11 at% over a thickness of 0.2 μm gives a dose of 2 X $10^{17}N/cm^2$. The smallest IS (0.15 mm/s) and QS (0.22 mm/s) (Table 11) are obtained in S4-2 in comparison with S8-1 (IS = 0.26 mm/s, QS = 0.28 mm/s) and S9-1 (IS = 0.21 mm/s, QS = 0.22 mm/s). One possible explanation is that the amount of N in solution may affect the IS and QS. Higher N in solution will yield an increased IS and QS. This result is consistent with a study of pure Fe-N samples [44].

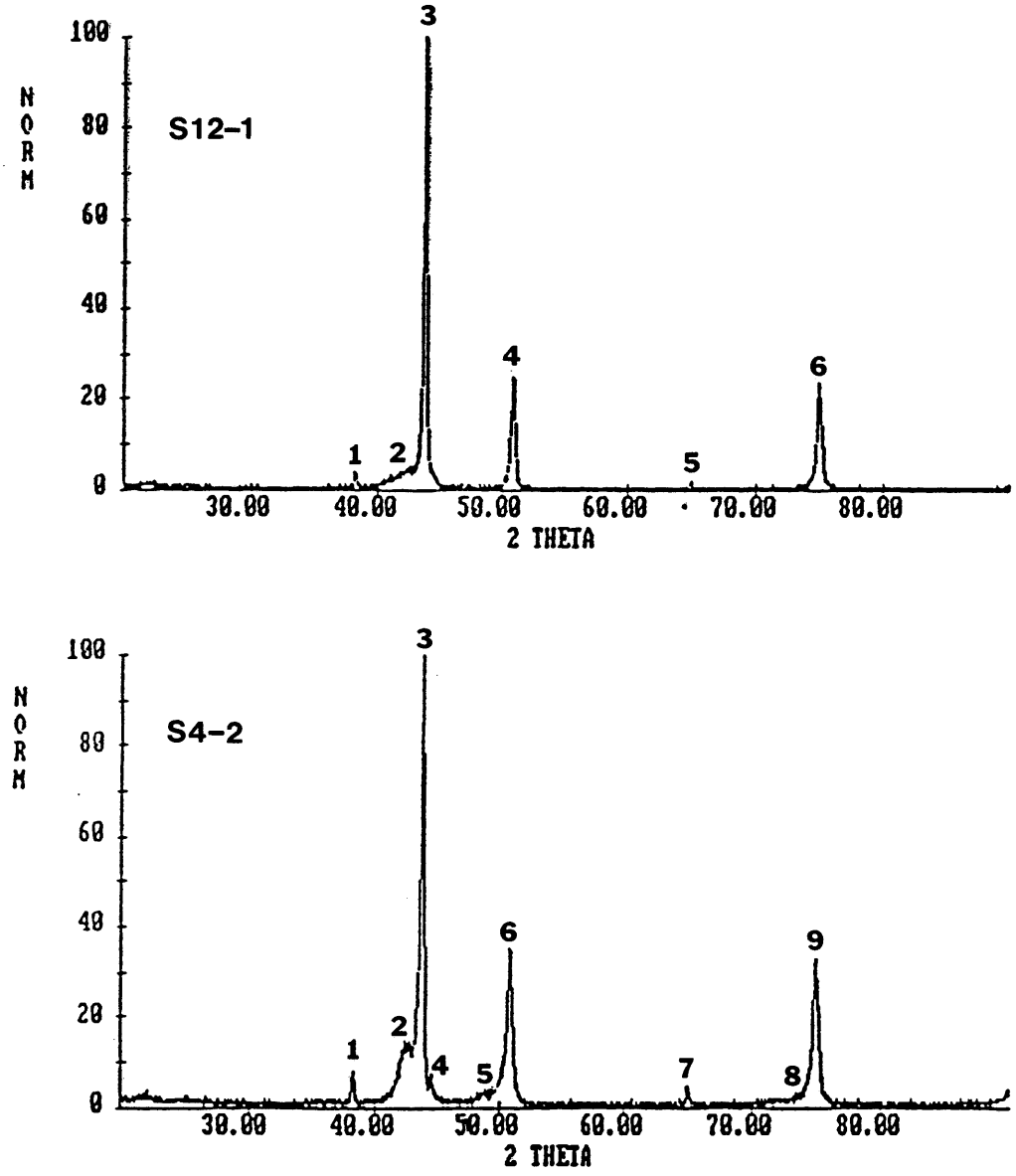

Fig. 16 XRD Data of S12-1, S4-2

TABLE 12 X-RAY DATA FOR IMPLANTED SAMPLES S12-1, S0-2 AND S4-2

Sample #	#	2θ	d(Å)	I	Phase	Δd/d
S12-1	1	38.50	2.336	3.0	Al(111)	
	2	42.31	2.132	3.5	Fe_2N	
	3	43.76	2.067	100	γ(111)	
	4	51.05	1.787	25.5	γ(200)	
	5	64.8	1.437	2.0	Al(220)	
	6	74.77	1.267	22.8	γ(220)	
S0-2	1	42.31	2.132	4.6	ϵ	
	2	43.70	2.070	100	γ(111)	
	3	44.81	2.020	7	Al(200)	
	4	51.05	1.787	80	γ(200)	
	5	74.77	1.267	53.0	γ(220)	
S4-2	1	38.50	2.336	8.9	Al(111)	
	2	42.31	2.132	14.5	γ_N(111)+ϵ	0.030
	3	43.70	2.070	100	γ(111)	
	4	44.81	2.020	6.2	Al(200)	
	5	49.80	1.829	3.4	γ_N(200)	0.024
	6	51.05	1.787	36.6	γ(200)	
	7	64.78	1.437	6.2	Al(220)	
	8	73.52	1.286	3.4	γ_N(220)	0.015
	9	74.77	1.267	33.8	γ(220)	

The AES depth profiles for samples S0-2 and S4-2 are shown in Fig. 17. The total nitrogen in S0-2 can be estimated under the N profile to yield 3 X 10^{17} N/cm^2. This value is larger than the total implanted nitrogen (1.7 X 10^{17} N/cm^2) demonstrating that there is a miscalibration of the AES concentration. Fig. 17 shows that the maximum N concentration in S4-2 is about 21 at.% and that the width of the N distribution (distinctly non-gaussian) at half maximum is about 1100 Å. The difference between the CEMS value of D = 450 Å and the AES profile width is attributed to radiation enhanced diffusion, since thermal diffusion yields a diffusion length $\sqrt{D_T t}$ of only 3 Å using T = 613 K and t = 32 s for sample S0-2 (Table 2). Comparing the two AES plots, nitrogen diffused deeper into S4-2 than S0-2. One reason for this is that the implantation temperature for S0-2 is 340±50°C which is lower than an apparent critical temperature of 380±50°C where all samples show the formation of N in solution due to an enhanced diffusion mechanism. Thus, the N in solution phase is associated with deep penetration of the N. From the CEMS data, we notice that the CEMS fraction of paramagnetic phase for S4-2 is much larger than S0-2. It suggests that the N in solution is much deeper than the nitride. Therefore, this is consistent with the AES profile. The maximum N concentration of S4-2 is about 21 at.% and the width of the N distribution at half maximum is about 2100 Å. The value is very close to the XRD study. The total nitrogen in S4-2 is 3.2 X 10^{17}ions/cm^2 (implanted one should be 1.7 X 10^{17}ions/cm^2) based on the estimation

under the N profile. Again this suggests that something is wrong with the AES calibration of atomic concentration and indicates that the quantitative values from the AES profiles must be used with caution.

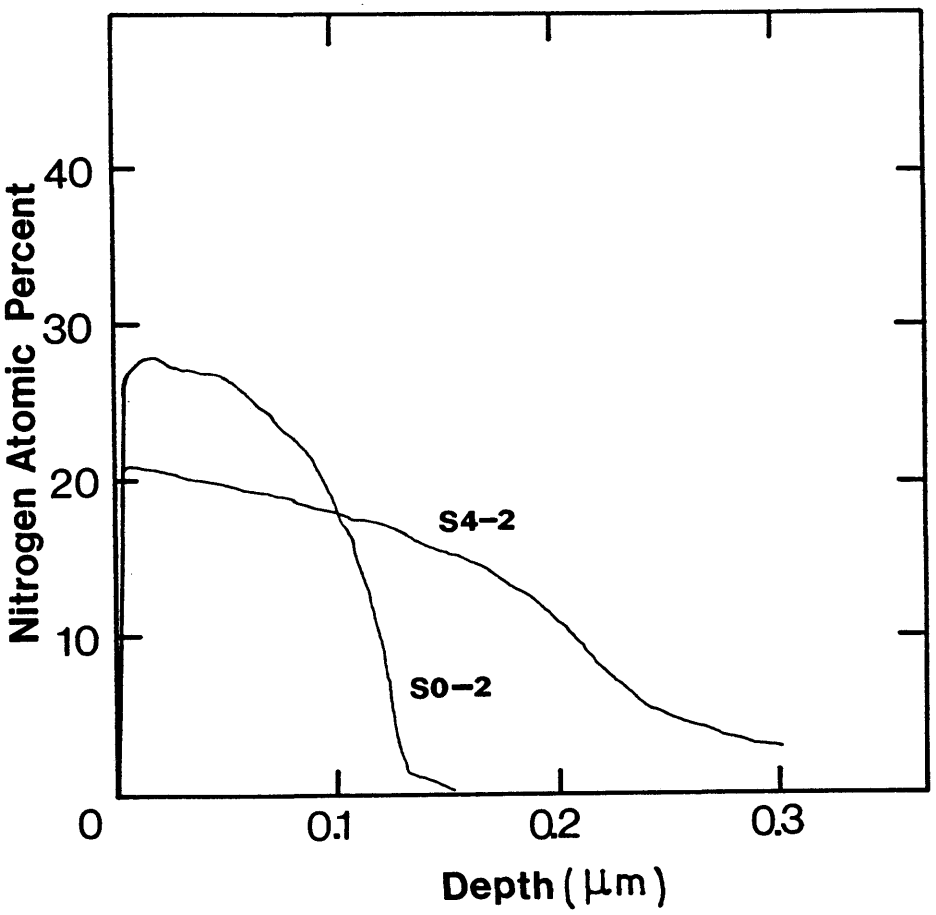

Fig. 17 AES Data of S0-2 and S4-2

4.2.4 $0.5X10^{17}$ ions/cm^2

Fig. 18 shows the CEMS from the two samples S1-1 and S7-1 implanted with this lowest dose. The effect of the N is to produce a poorly resolved paramagnetic resonance shifted by about +0.3 mm/s from the austenite resonance. No magnetic nitride phase was detected under this implanted condition. The results in Table 13 show that the paramagnetic resonance from the two samples has a different IS and QS.

X-ray diffraction show that there is one well defined peak at 2θ = 42.3 degrees (d = 2.14 Å) from the 280°C sample. This value of d is close to the (111) planar spacing in hexagonal ϵ-(Fe, Cr ,$Ni)_{2+x}N$ compounds with x = 0 to 1 similar to S0-2. The (111) peak is the strongest one in the ϵ-(Fe, Cr, $Ni)_{2+x}N$ powder pattern [37] but no other peaks could be detected in this sample. This again suggests a strong preferred orientation of the (111) planes parallel to the surface of the disc. The XRD from sample S7-1 shows broad, weak peaks at 2θ = 42.5 and 49.4° corresponding to d = 2.12 and 1.84 Å. These spacings correspond to an expanded austenite lattice caused by N in solution. Comparing the CEMS and XRD studies, we find that the FeNP of S1-1 (IS = 0.16 mm/s and QS = 0.11 mm/s) is a nitride which is different from that in S0-2 (IS = 0.18 mm/s and QS = 0.23 mm/s). The FeNP of S7-1 is N in solution with a slightly higher IS (0.19) than that of S4-2 (IS = 0.15). The average content of nitrogen in solution is 12 at% based on the above d spacings and equation 3.

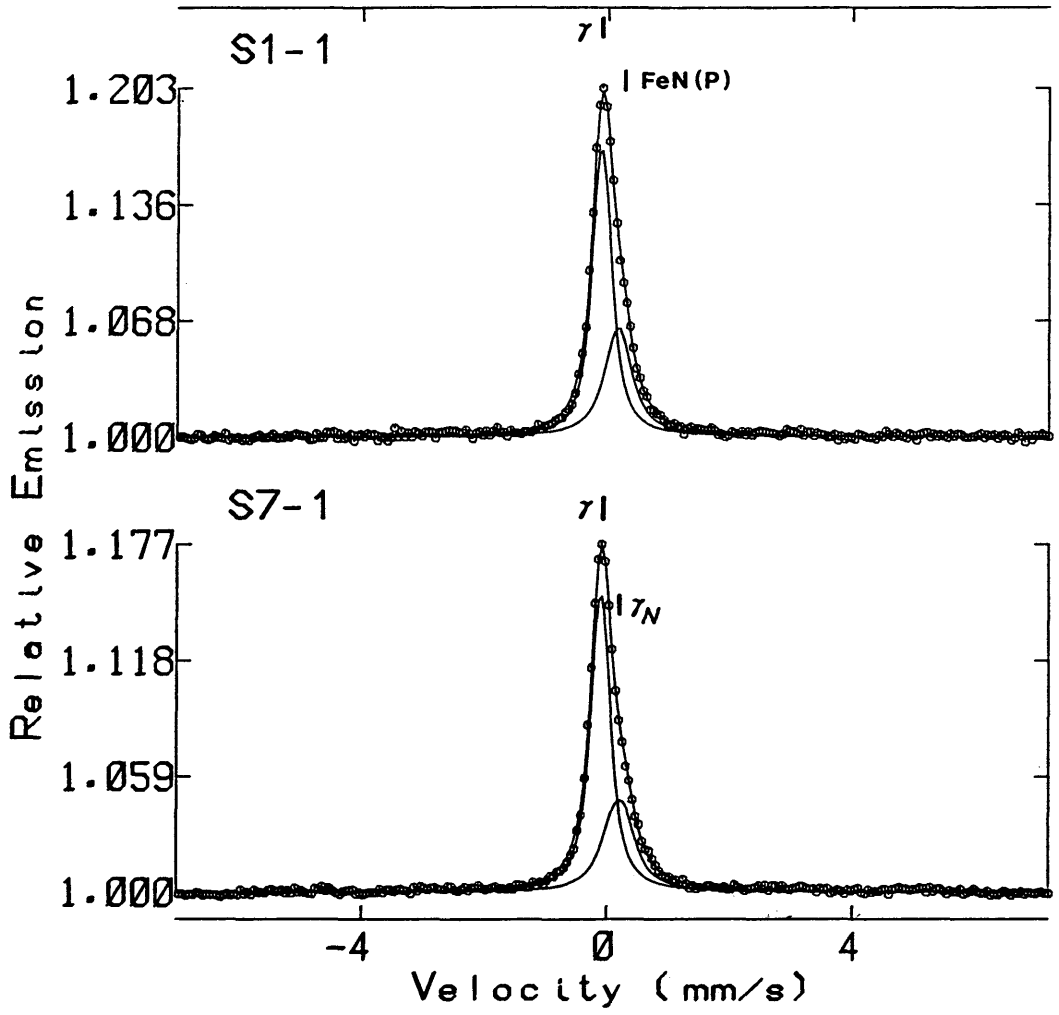

Fig. 18 CEMS of S1-1 and S7-1

TABLE 13. CEMS PARAMETERS FOR S1-1 AND S7-1

Sample No.	Phase	IS (mm/s)	QS (mm/s)	W_{34} (mm/s)	H (T)	F (%)	D (μm)
S1-1	γ	-0.108(f)	0.13(1)	0.3(f)		64(1)	
	FeNP	0.16 (1)	0.11(1)	0.5(f)		36(1)	.05
S7-1	γ	-0.108(f)	0.12(1)	0.3(f)		67(1)	
	γ_N	0.19 (1)	0.19(2)	0.5(f)		33(1)	.09

The thickness of the paramagnetic nitride layer of S1-1 is calculated from the CEMS fraction and the theory used to generate the curves of fig. 3 [27]. With the assumption that the nitrogen-containing phase is uniform from the surface to a depth D, then D = 450 Å is obtained for S1-1. The depth of the layer of the nitrogen in solution of S7-1 is about 0.09 μm based on equation 4.

The AES sputter depth profile of S7-1 is shown in Fig. 19. This profile shows that the peak concentration of nitrogen is approximately 23 at%, which occurs at about 480 Å. The latter is in good agreement with the mean range of 430 Å calculated in section 3.2 for the 60 keV implantation energy used here. The width of the N distribution at half maximum is about 850 Å which is much larger than the predicted width of the implantation profile (430 Å). Since the prediction does not include a diffusion mechanism, it is suggested that this is the cause of the much broader experimental N distribution. The thermal diffusion length ($\sqrt{D_T t}$) of sample S7-1 (Table 2) is only about 20 Å using T = 670 K and t = 80 s. Therefore, radiation enhanced diffusion plays a major role in this sample. The total nitrogen retained in this sample is about 1.4 X 10^{17}N/cm^2 based on the estimated area under the N profile. This value is larger than the implanted value of 0.85 X 10^{17}N/cm^2. Again, this suggests a miscalibration of the AES concentration.

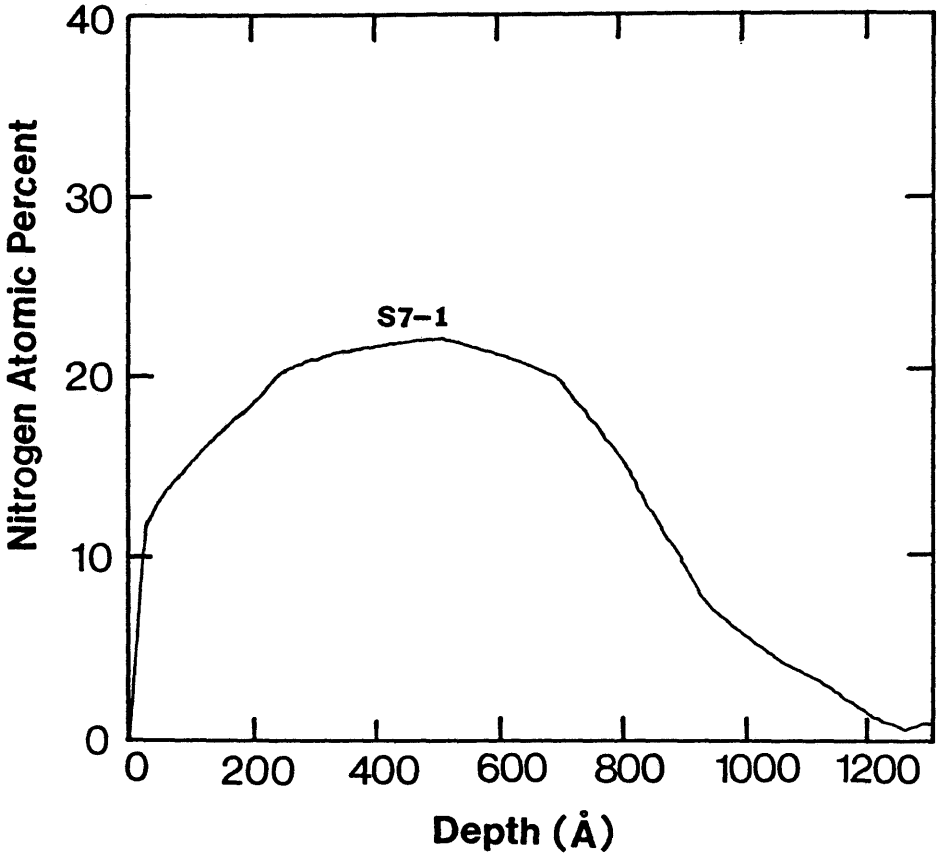

Fig. 19 AES Data of S7-1

4.3 AS-IMPLANTED 310 SS SAMPLES

From our previous discussion of implanted 304 SS samples, we found that total dose and implantation temperature are important factors for phase formation. Thick N in solution layers were found in the samples implanted at temperatures 380±50°C. Therefore, the 310 SS (Table 2.) samples were all implanted at this temperature and with the total dose ranging from 0.5 X 10^{17} to 10 X 10^{17} ions/cm^2. Fig. 20 shows CEMS data of samples T1-2, T0-1, T2-1 and T3-1. A paramagnetic phase was detected in T3-1 and T1-2. A magnetic phase begins to appear at 1 X 10^{17} ions/cm^2 and increased with increasing dosage. No α'(martensite) phase was obtained because of the higher Cr and Ni which stabilized the phase as discussed earlier relative to the polishing and wear of unimplanted samples. Table 14 lists CEMS parameters for the implanted 310 SS samples. The austenite IS and W of 310 SS were fixed at the known unimplanted values. In order to obtain a good comparison, the fixed W of N and FeNM were based on the 304 SS results. IS and QS of T3-1 show that the paramagnetic phase is similar to Fe_2N Smaller hyperfine fields in T0-1, T2-1, and T3-1 than that of 304 is due to the higher Cr concentration in solution (Table. 1).

Table 15 lists XRD data for 310 SS. XRD measurements for T1-2 and T0-1 are shown in Fig. 21 and peaks 1, 4, 7, and 10 in T1-2 are due to the Al sample holder. Peaks 2, 5, and 8 in T1-2 are expanded γ(111), γ(200), and γ(220), respectively. Therefore, the paramagnetic phase is at least partly due to nitrogen in solution. The average

amount of nitrogen in solution is about 8% based on equation 3.

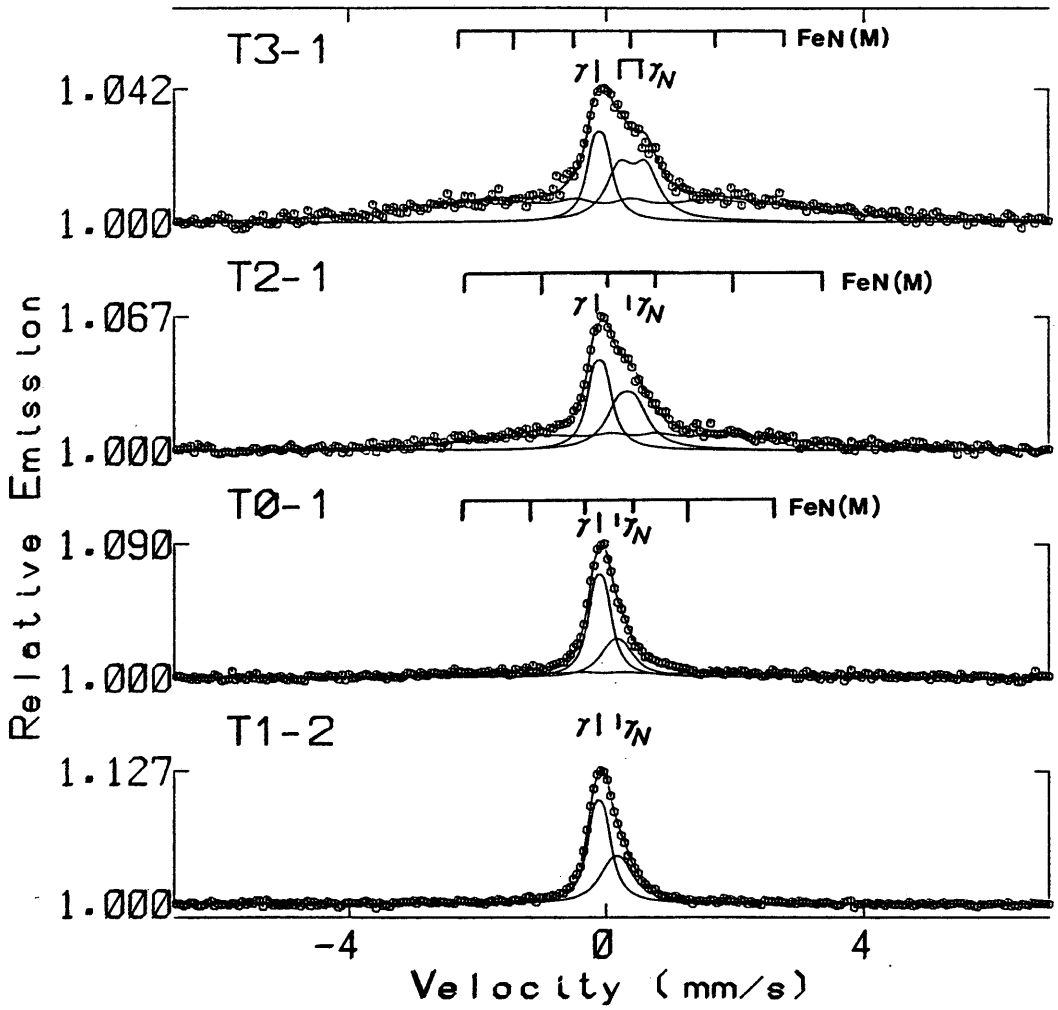

Fig. 20 CEMS of T1-2, T0-1, T2-1, and T3-1

TABLE 14. CEMS PARAMETERS FOR T1-2, T0-1, T2-1, AND T3-1

Sample No.	Phase	IS (mm/s)	QS (mm/s)	W_{34} (mm/s)	H (T)	F (%)	D (μm)
T1-2	γ	-0.104(f)	0.16(1)	0.3(f)		59(1)	
	γ_N	0.17 (1)	0.18(1)	0.5(f)		46(1)	.24
T0-1	γ	-0.104(f)	0.16(2)	0.3(f)		48(2)	
	γ_N	0.17 (2)	0.18(4)	0.5(f)		26(1)	0.2
	FeNM	0.06(6)	0.00(f)	0.7(f)	13.5(6)	25(2)	
T2-1	γ	-0.104(f)	0.17(1)	0.3(f)		26(1)	
	γ_N	0.32 (1)	0.26(1)	0.5(f)		26(1)	0.7
	FeNM	0.43 (6)	0.00(f)	0.7(f)	13.6(4)	48(2)	
T3-1	γ	-0.104(f)	0.17(f)	0.3(f)		18(1)	
	$\gamma_N+\epsilon$	0.41 (1)	0.41(1)	0.5(f)		25(1)	1.6
	FeNM	0.05(3)	0.00(f)	0.7(f)	16.9(4)	57(2)	

TABLE 15 X-RAY DATA FOR IMPLANTED SAMPLES T1-2, T0-1, T2-1 and T3-1

Sample #	#	2θ	d(Å)	I	Phase	Δd/d
T1-2	1	38.03	2.360	10.0	Al(111)	
	2	42.50	2.125	11.0	γ_N(111)	0.026
	3	43.57	2.072	100	γ(111)	
	4	44.29	2.040	4.0	Al(200)	
	5	49.64	1.831	10	γ_N(200)	0.018
	6	50.71	1.799	52	γ(200)	
	7	64.64	1.440	4	Al(220)	
	8	73.57	1.284	5	γ_N(220)	0.011
	9	74.64	1.270	59	γ(220)	
T0-1	1	43.14	2.093	20.0	γ_N(111)	0.012
	2	43.75	2.069	100	γ(111)	
	3	50.00	1.823	5.0	γ_N(200)	0.019
	4	51.00	1.789	66	γ(200)	
	5	73.00	1.295	6.2	γ_N(220)	0.018
	6	74.50	1.272	68.0	γ(220)	
T2-1	1	38.17	2.356	15.0	Al(111)	
	2	41.90	2.150	67.0	γ_N(111)+ϵ	0.036
	3	43.54	2.075	100	γ(111)	
	4	44.37	2.038	5.0	Al(200)	
	5	48.50	1.875	12.0	γ_N(200)	0.041
	6	50.57	1.802	68.0	γ(200)	
	7	64.61	1.441	7.0	Al(220)	
	8	71.63	1.318	5.0	γ_N(220)	0.026
	9	73.69	1.284	80.0	γ(220)	
T3-1	1	38.57	2.330	15.0	Al(111)	
	2	41.61	2.167	100	γ_N(111)+ϵ	0.044
	3	43.57	2.075	42.0	γ(111)	
	4	44.29	2.043	5.0	Al(200)	
	5	47.86	1.897	18.0	γ_N(200)	0.054
	6	50.71	1.799	31.0	γ(200)	
	7	64.82	1.437	7.0	Al(200)	
	8	71.79	1.313	8.0	γ_N(220)	0.033
	9	74.64	1.271	47.0	γ(220)	

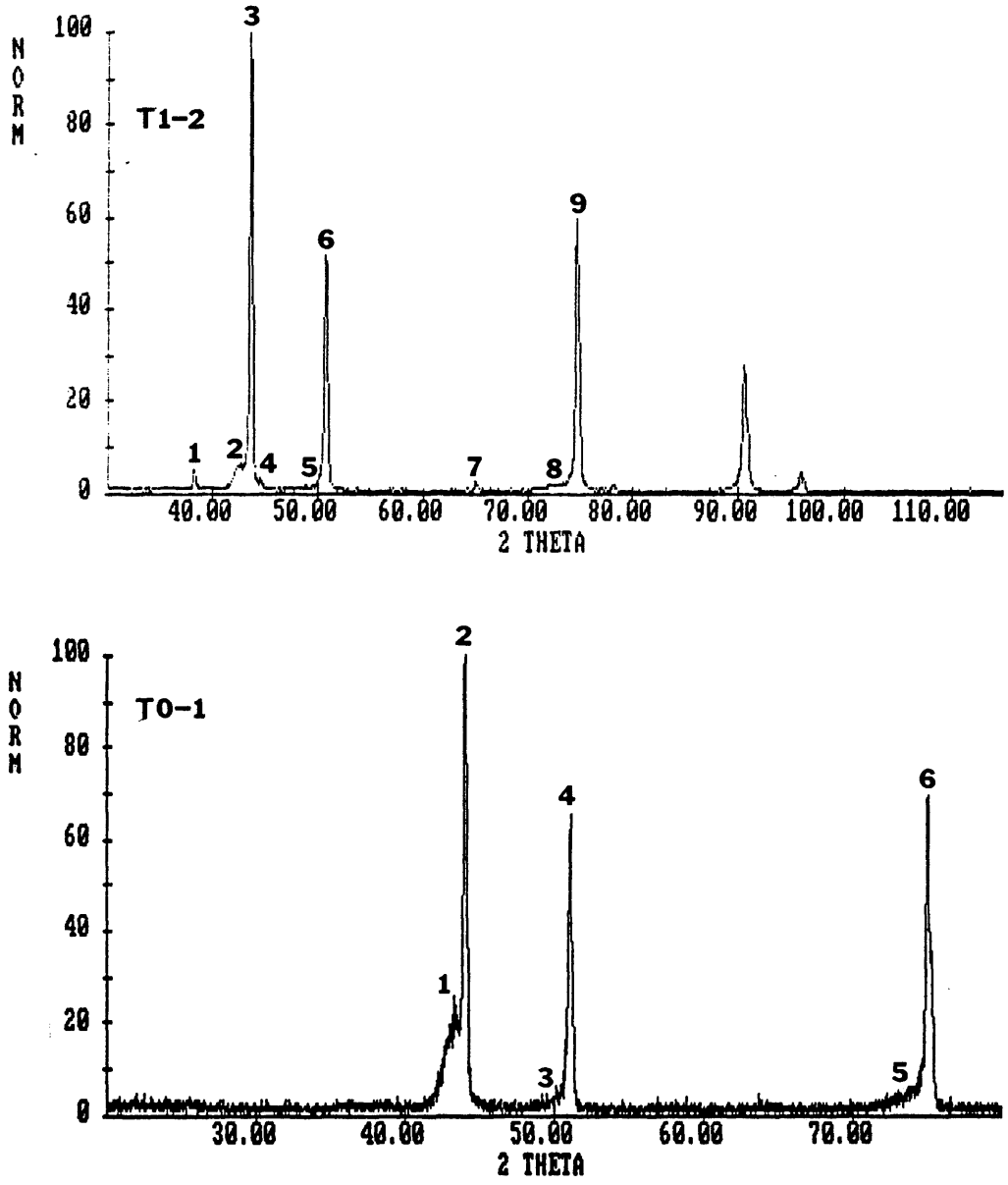

Fig. 21 XRD Data of T1-2 and T0-1

The thickness of N in solution layer can be estimated based on equation 4 using peaks 5 and 6 and it is about 0.24 μm. The reason for using these two peaks for the calculation of layer of N in solution is that there may be magnetic or paramagnetic nitride phases which affect peak 2 formed in the sample. XRD measurement of T0-1 shows a well defined peak 1 at 42.4 degree (d = 2.14) which corresponds to ϵ-(Fe, Cr, $Ni)_{2+x}N$ with x = 0 to 2. In addition to the well defined peak 1, the broading of the peak is due to a contribution from a γ(111) expansion peak. Peaks 3 and 5 are attributed to the expansion of γ(200) and γ(220), respectively. The concentration of N in solution is about 7.5 % and the thickness of the N in solution layer is about 0.2 μm.

Fig. 22 shows XRD data for T2-1 and T3-1. It is obvious that there is more N in solution in these two samples. Athough the CEMS data show the presence of a Fe_2N-like nitride, this must be near the surface when the N concentration is highest. The XRD Fe_2N-like peak is obscured by the γ_N(111) peak. Under the peak 1 (due to Al) on both samples there is a small broad peak which due to the ϵ-(Fe, Cr, $Ni)_{2+x}N$ with x = 0 to 2 [37] along with the peak 2 for both samples. Therefore, peaks 5 and 6 were chosen for the calculation of the N in solution layer thickness. They are about 0.7 μm and 1.6 μm for T2-1 and T3-1, respectively. The N concentrations are about 16 at% and 20 at% based on Δd/d from table 15 for T2-1 and T3-1, respectively.

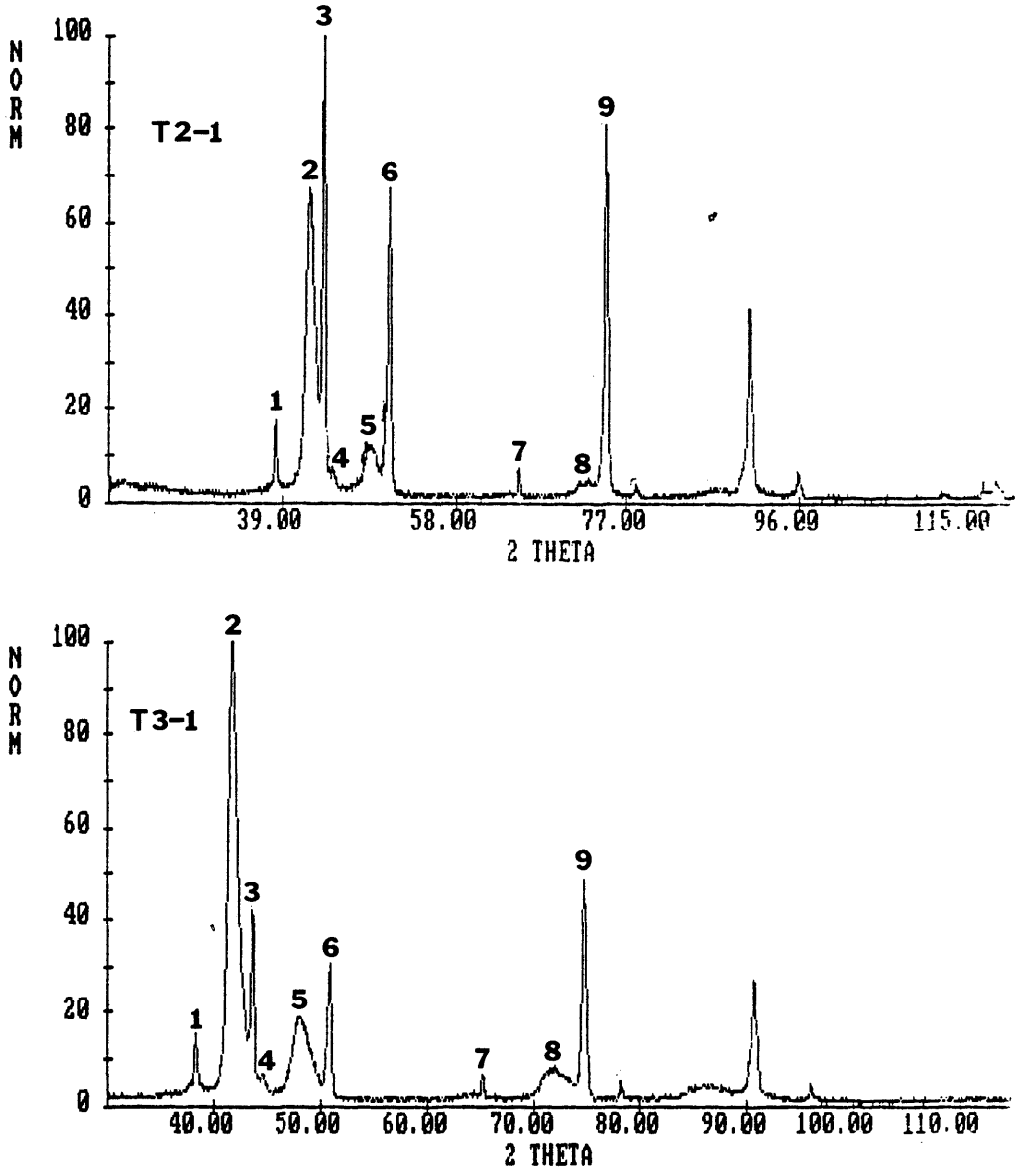

Fig. 22 XRD Data of T2-1 and T3-1

4.4 OSCILLATING PIN-ON-DISC WEAR TESTING OF IMPLANTED SAMPLES

Results of wear testing show that implanted samples have a wear rate that is too small to be detected. This is illustrated in Fig. 23 for sample S3-1 in comparison with an unimplanted sample. All of the implanted samples have a similar wear behavior. Wear testing on both was done with an applied normal load of 1 N under the lubricated condition. The results show that the unimplanted disc wears at a normalized rate near 1 mg/N/h while the implanted sample shows a mass loss less than the measurement uncertainty (±11 μg) after 30 hr.

Fig. 24 shows wear data from S9-1 as a typical example of the wear test procedure. Since all of the implanted samples show no detectable adhesive wear while the unimplanted ones show severe adhesive wear, a test was designed in order to find the transition from no wear to severe adhesive wear. The load is gradually increased in one to two Newton increments and worn for about one hour at each load. This is repeated until a sudden increase in wear occurs as shown in Fig. 24 and this determines the critical load. Table 16 lists the critical loads for all samples. The critical load increases systematically with increasing dose at the temperature 380±50°C as shown in Fig. 25. For 304, the critical load increased monotonically with increasing the total dose, whereas for 310 , approximately the same critical load was found for 1 and 4 X 10^{17} ions/cm^2 . This shows that the martensite content produced during the surface finishing of 304 SS or its reduced stability with respect to the austenite-martensite transformation are not important

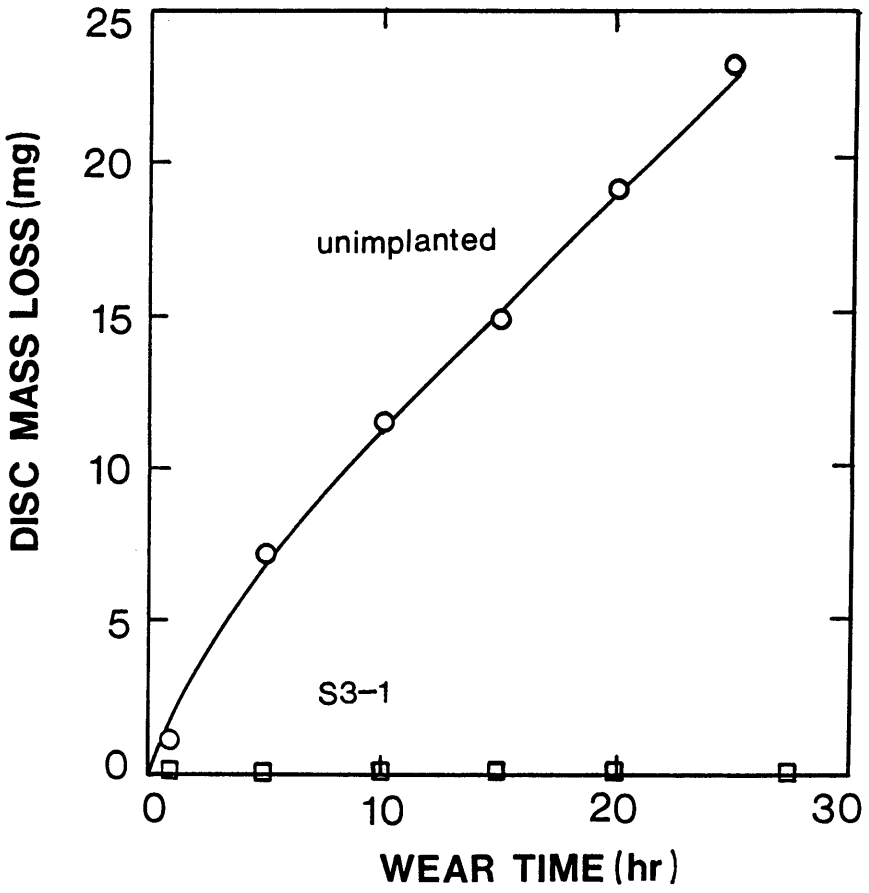

Fig. 23 Wear Test Data of implanted and unimplanted 304 SS

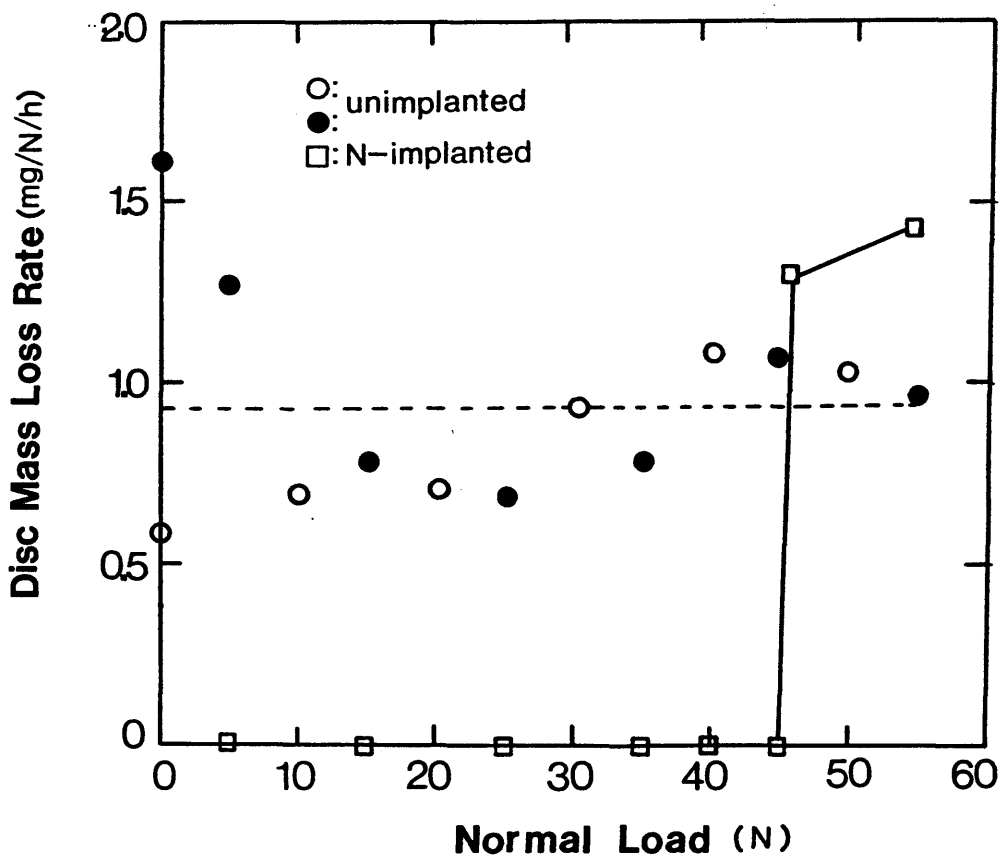

Fig. 24 Wear Data of S9-1 and unimplanted 304 SS

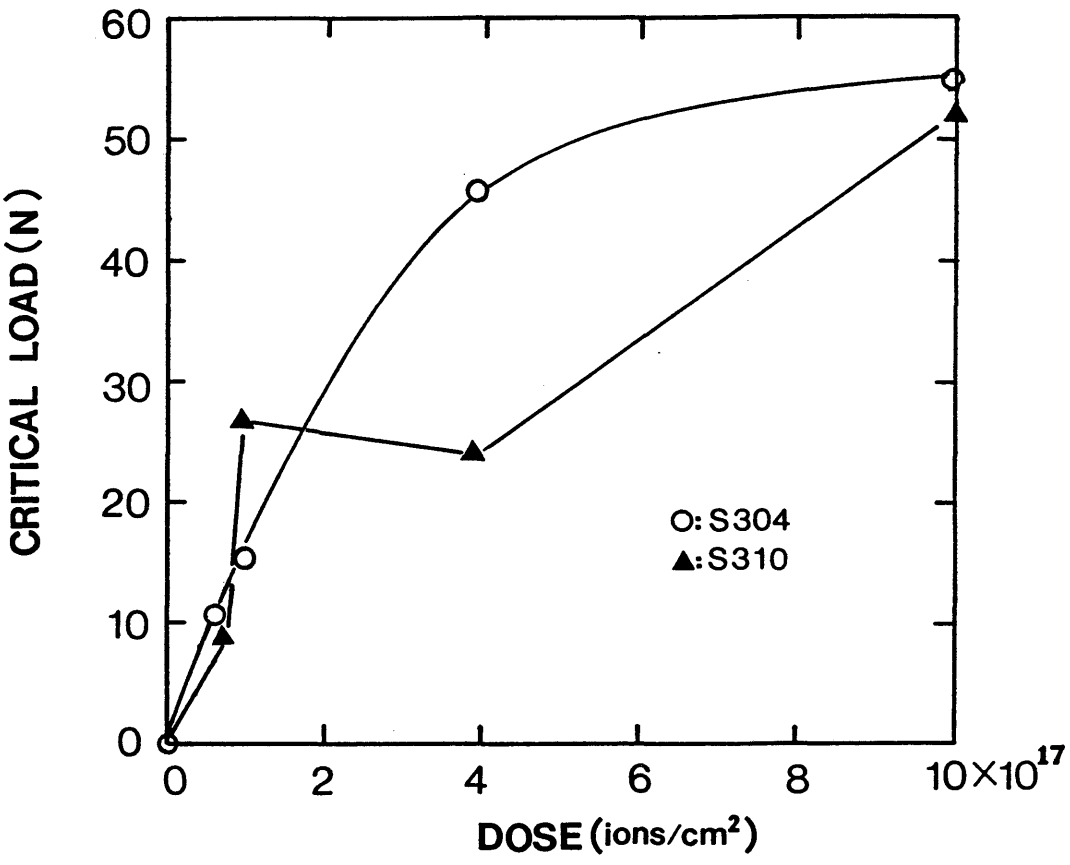

Fig. 25 Critical Load vs. Total Dose of 304 SS and 310 SS.

The solid lines are drawn to quide the eye.

factors in increasing the surface hardness of implanted 304 SS. This is in contrast to our earlier results which showed a significantly higher wear rate for unimplanted 304 SS compared to 310 SS (Fig. 8). Table 16 also includes a summary of the microstructural results for each sample. Note that the critical load at 380°C also scales systematically with the thickness of the γ_N phase.

Samples S1-1, S7-1, S3-1 and S8-1 were also studied by CEMS during or after wear testing. After a 1 h wear test at a load of 5 N on S1-1, CEMS data in Fig. 26 show that martensite formed after the hard layer was broken through (i.e., above the critical load) and no nitride remains. By comparison with Fig. 5 (wear testing of as-polished, unimplanted sample) both CEMS patterns after wear testing are very similar.

Fig. 27 shows CEMS data after two stages of wear testing of S7-1. At lower load (less than 10 N), there was no detectable mass loss. When the wear load increased to 10 N, mass loss began to occur after 3 hours wear (wear depth is about 410 Å). At this stage, the CEMS data shows that there is martensite formed and that some of the γ_N phase remains. It suggests that martensite forms in association with the initial stages of increased wear when the hard layer begins to be removed. After the 5 h wear test at the same load, wear testing was stopped just after the mass loss rate rose dramatically indicating that all beneficial effects of the hard layer were lost. The CEMS data shows no

TABLE 16 Critical Loads For 304 Stainless Steels (Lubricated, Oscillating Pin Tests)

Disc No.	Total Dose (10^{17} ions/cm2)	Temp. (°C)	Phases (D= μm)	Crit. load (N)
S0-1	0	0	α'+	≤0.1*
S5-1	0	0	α'+	≤0.1**
S1-1	0.5	280	FeNP	≤5
S7-1	0.5	400	γ_N(0.09)	10
S12-1	1	160	Fe_2N	11
			ε	
S0-2	1	340±50	FeNP	5
S4-2	1	380±50	γ_N(0.2)	14
S3-1	4	350	Fe_2N	15
			ε	
S9-1	4	380±50	γ_N(0.6)	46
			ε	
S8-1	10	380±50	γ_N(1.4)	55
			ε	
			α-Fe	
T1-1	0	0		≤0.1
T1-2	0.5	380±50	γ_N(0.24)	9
T0-1	1	380±50	γ_N(0.2)	27
			ε	
T2-1	4	380±50	γ_N(0.7)	24
			ε	
T3-1	10	380±50	γ_N(1.6)	52
			ε	

* lightest load used on this sample.

** Smallest load possible with apparatus.

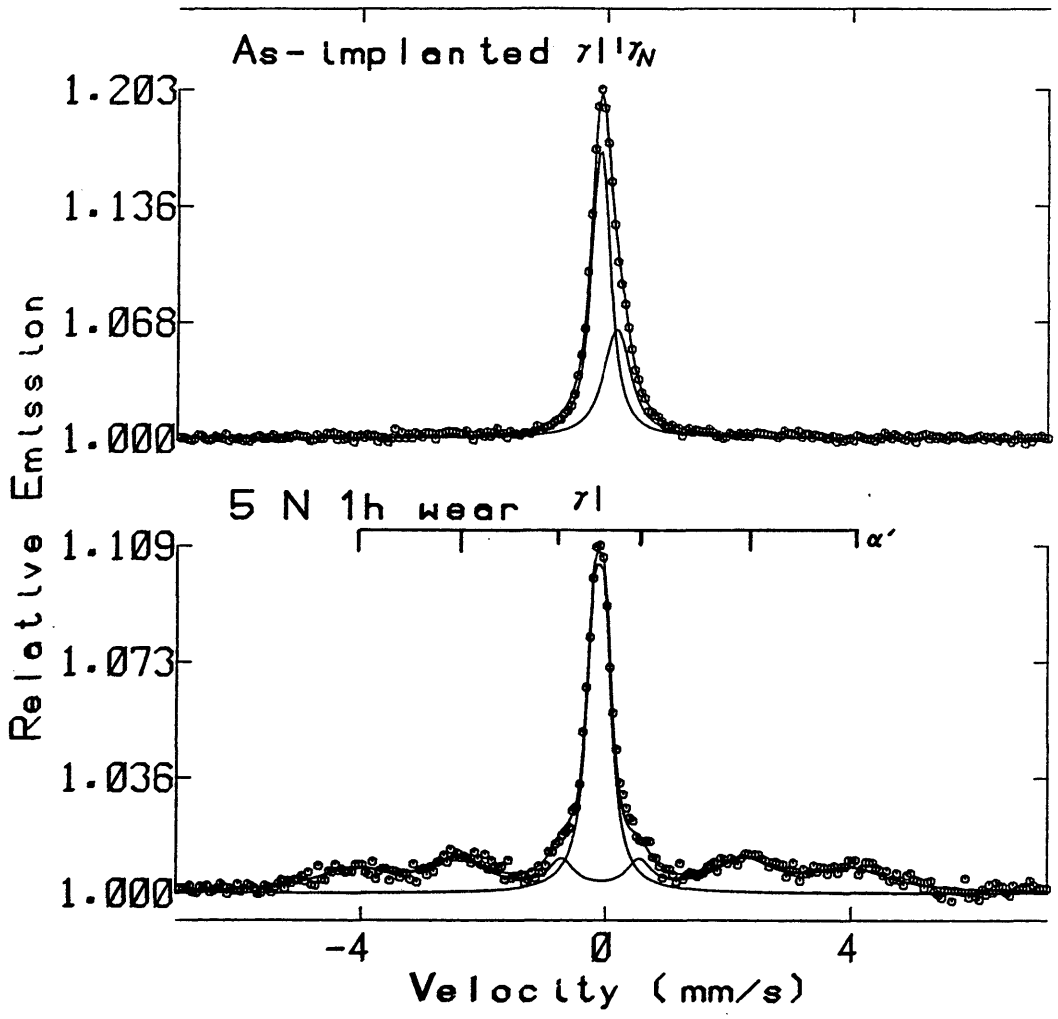

Fig. 26 CEMS Data of S1-1 after 1 h wear at the load of 5 N

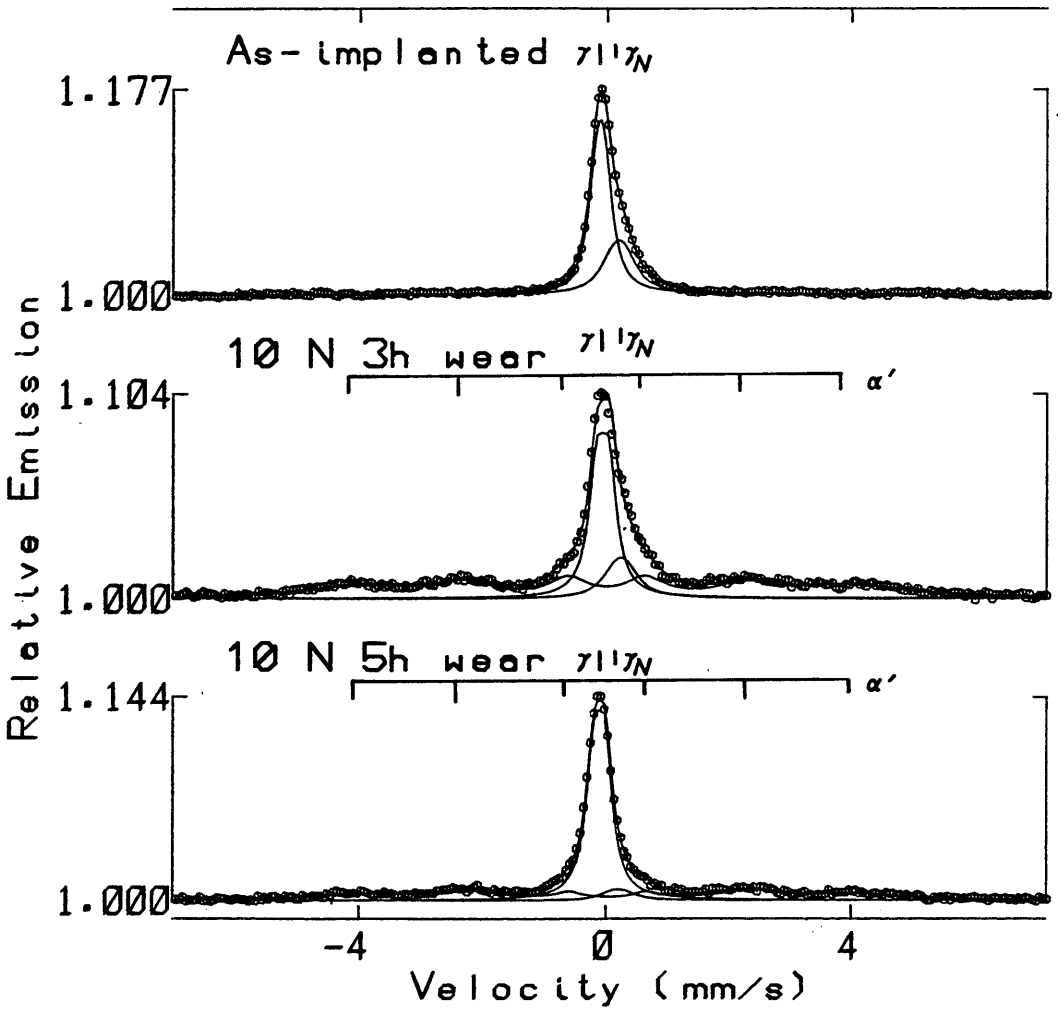

Fig. 27 CEMS Data of S7-1 after 3 h and 5 h wear at the load of 10 N

evidence of the γ_N phase and less martensite obtained by comparison with 3 h wear testing. This is suggested to be due to partial support of the load by the hard layer so that strain-induced martensite phase forms near the surface during the wear testing. After the hard layer is broken through, more strain-induced martensite appear deeper as discussed earlier (Fig. 6).

Fig. 28 shows CEMS data after two stages of wear on S3-1. Two hours wear testing at the load of 10 N was done with no detectable mass loss, and the pattern looks very similar to the as-implanted one. This shows that the wear process has not induced phase changes in the nitride layer nor the formation of martensite below this layer. Mass loss began to occur after 2 hours wear testing at the critical load of 15 N. Martensite was obtained and a small amount of $(Fe, Cr, Ni)_2N$ remained. At this condition the hard layer is not broken through. From Table 16 we see that in this case the critical load is slightly higher than S4-2 even though the total dose is 4 times bigger than S4-2. It suggests that a thin nitride Fe_2N phase is not as effective as a thicker layer of the N in solution phase.

The Vickers microhardness values (Hv) of the samples were measured at CSU by using an ultralight load microhardness tester. The results are given in Fig. 29. Compared to the unimplanted samples (both as-received and polished) the implanted samples yield a higher surface hardness (detectable at the smallest loads). This is attributed to the N in solution resulting from the N implantation.

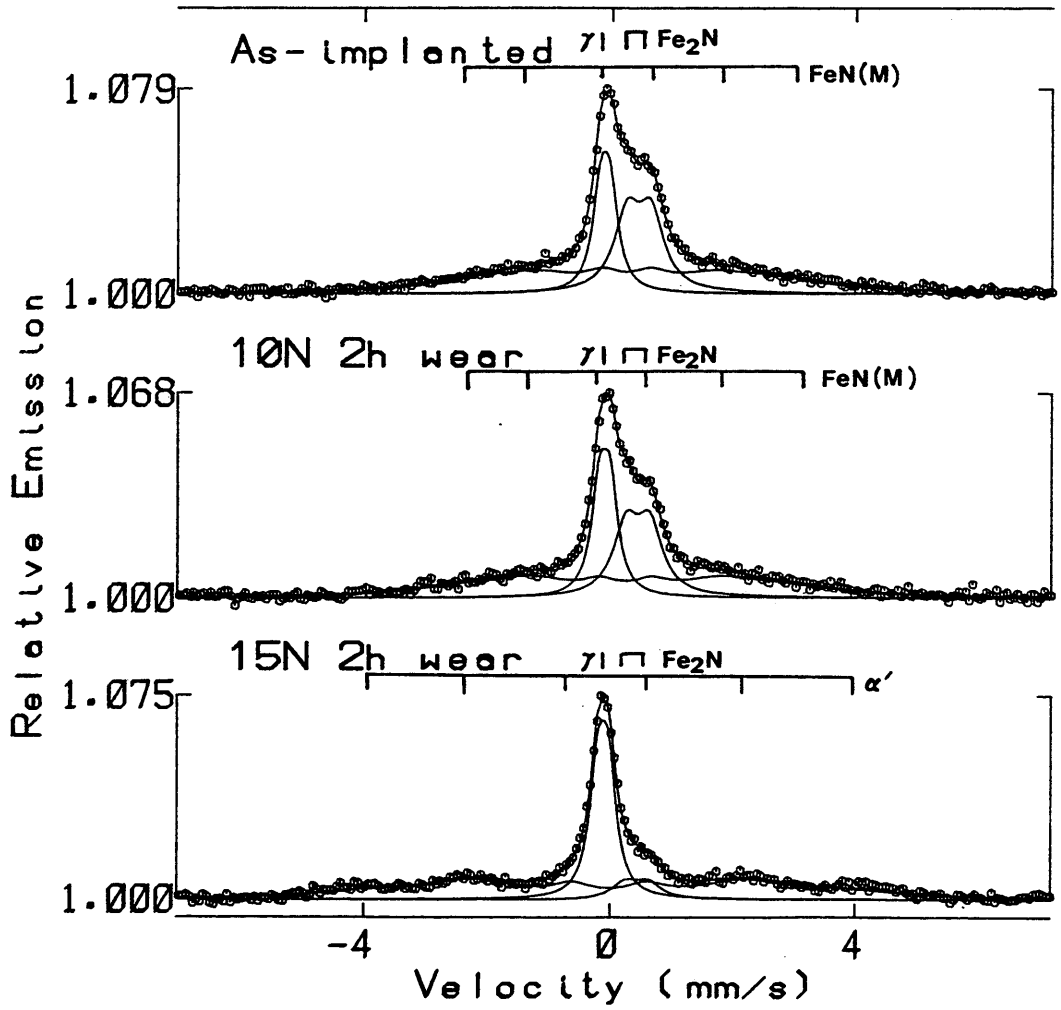

Fig. 28 CEMS Data of S3-1 after 2 h wear at the load of 10 N and 15 N

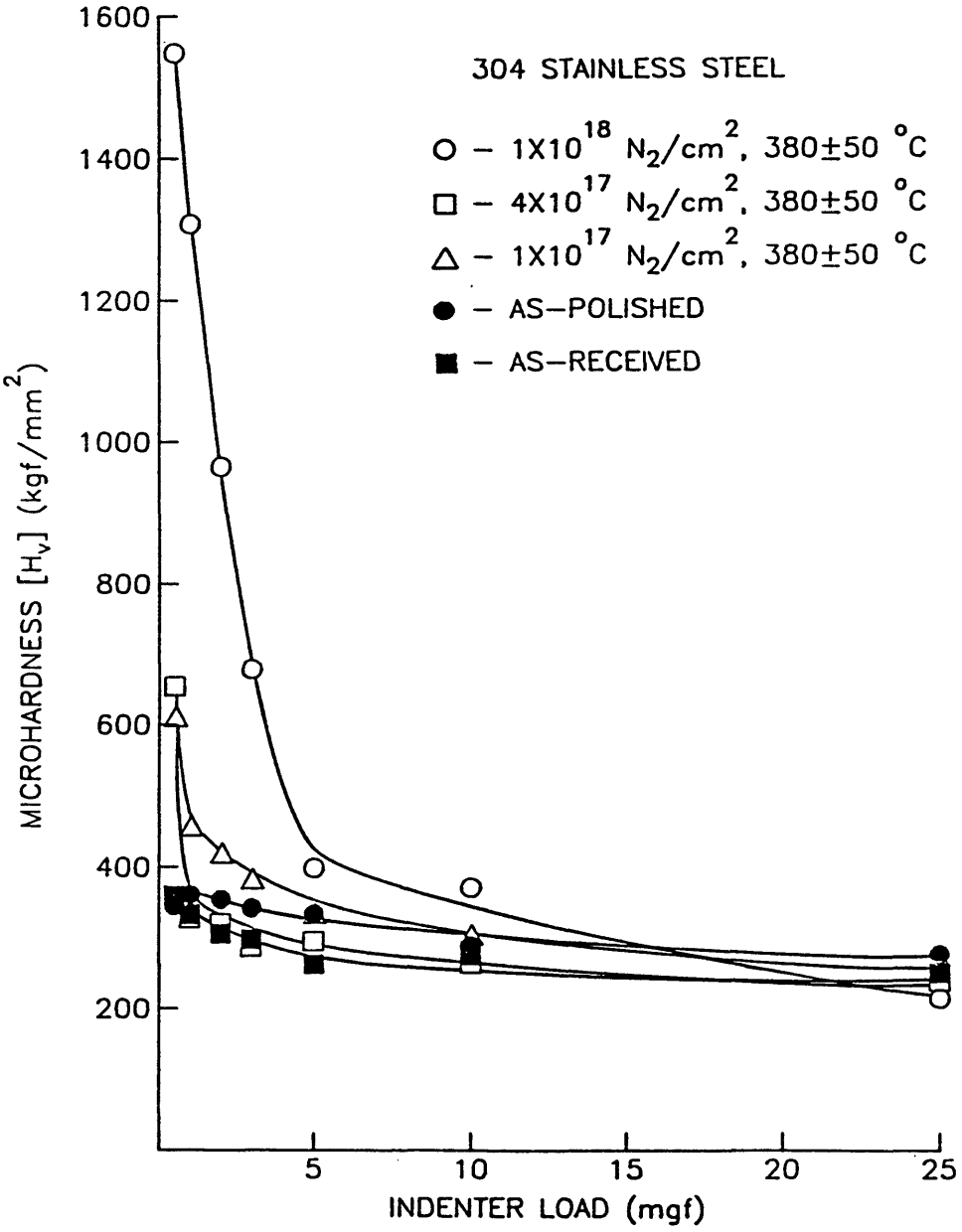

Fig. 29 Microhardness Data of 304 SS

Our laboratory studies of solid solution hardening (due to the change of wear behavior from severe to mild and the higher surface hardness) can be directly connected with studies of solid solution hardening and strengthing of nitrogen alloyed austenitic SS [47,48]. Fig. 30 shows the plots of the stresses of 304 calculated based on the critical load and pin mass loss and the yield stress from Fig. 1b [47] vs. nitrogen content. The extrapolated dished line is based on ref[48]. It shows that the increase in stress is proportional to the square root of the N concentration in the solution. Therefore, with 16 at.% N in solution, the stress should be approximately 1300 mpa, which is quite similar to our sample S9-1.

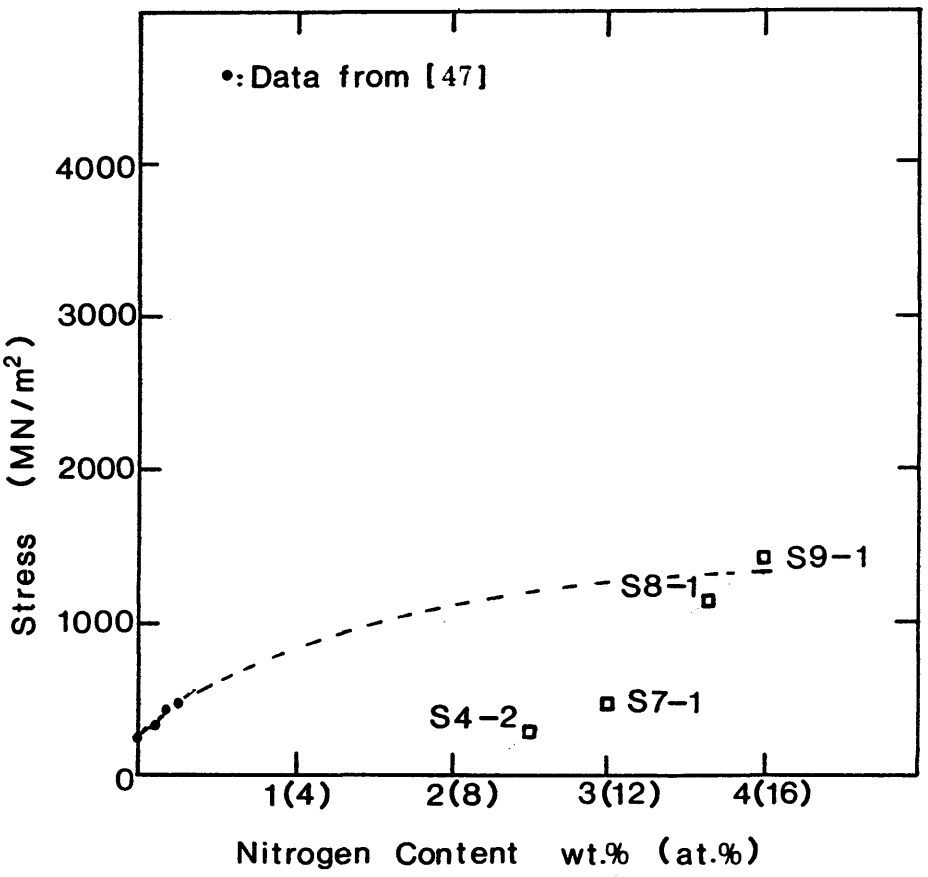

Fig. 30 Stress vs. Nitrogen Content

5. SUMMARY AND CONCLUSIONS

Nitrogen ion implantation into 304 and 310 stainless steel produces great improvements in their wear behavior. When the N-in-solution phase is achieved in the steel, the mild adhesive wear behavior is prolonged and the transition to severe wear behavior occurs at a greater critical load. The critical load for the implanted samples is two to three orders of magnitude greater than that for the unimplanted samples. To form the N-in-solution phase in the steel requires deep penetration of the implanted nitrogen. Deep penetration of implanted nitrogen can be achieved when the implantation temperature is equal to or higher than 380±50°C with the dose ranging from 0.5 X 10^{17} ions/cm^2 to 1 X 10^{18} ions/cm^2. The critical nature of this temperature for formation of the N-in-solution can be seen from the results for samples S3-1 and S0-2, which were implanted at temperatures of 350°C and 340±50°C, respectively, and no N-in-solution was detected by CEMS or XRD. The shallow penetration in S0-2 is confirmed by the AES profile. The phase formed at 350°C and below were found to be paramagnetic or magnetic nitrides with hexagonal structures rather than solid solutions. AES profiles provided the N distribution for some samples. The deeper penetration depth of N than the expected implanted depth of 430 Å is attributed to a radiation enhanced diffusion mechanism. Greater surface hardness at low indenter loads was obtained with increasing implanted dose at the temperature 380±50°C. These beneficial effects show that

the mechanism of solid solution hardening plays a major role in improving the wear behavior.

By comparison of the results from unimplanted 304 SS and 310 SS, the wear tests show that 310 SS has a lower wear rate than 304 SS and this is attributed to the transformation from austenite to martensite in 304 SS which causes a volume increase of about 5 %. This volumetric change probably produces microcracks which then leads to enhanced removal of the surface martensite by the wear pin. Wear debris studies confirm that 304 SS debris is highly enriched in α'-martensite and that 310 SS debris is paramagnetic. Transformation from austenite to martensite occurred only in 304 SS because of the higher austenite stability in 310 SS. Wear test results from implanted 304 SS and 310 SS show a similar increase in critical load with nitrogen dose. This suggests that the martensite content produced during the sample finishing or the reduced stability of austenite in 304 SS does not play an important role in affecting the wear behavior of N implanted 304 SS.

References

[1]. G. Dearnaley, in Ion Implantation Metallurgy, ed. by C. M Preece and J.K. Hirvonen (American Institute of Mining, Metallurgical and Petroleum Engineers, Inc. New York, 1980) p.1

[2]. Yi Qu, Master of Science Thesis, Colorado School of Mines, Thesis Number T-3616, 1988.

[3]. Ronghua Wei, Paul J. Wilbur, W. S. Sampath, D. L. Williamson, Yi Qu and Li Wang, J. Trib. (in press)

[4]. R. J. Raudebaugh, Introduction to Stainless Steels (Materials Engineering Institute, Metals Park, Ohio) Course 18, lesson, Test 1. p.18

[5]. K. L. Hsu, T. M. Ahn and D. A. Rigney, Wear 60 (1980) 13

[6]. W. Schumacher, in Proc. Int. Conf. on Wear of Materials, ed. by W. A. Glaeser, K. C. Ludema, and S. K. Rhee (United Engineering Center, New York 1977) p.134

[7]. Z. Y. Yang, M. G. S. Naylor and D. A. Rigney, Wear 105 (1985) 73

[8]. D. C. Cook, Metall. Trans. 18A (1987) 201

[9] G. Wagner, R. Leutenecker, T. Louis and U. Gonser, Hyperfine Interactions 42 (1988) 1017

[10]. T. Spalvins, Thin Solid Films 108 (1983) 157

[11]. L. O. Daniels and P. J. Wilbur, Nucl. Instrum. Meth. Phys. Res. B19/20 (1987) 221

[12]. W. C. Oliver, R. Hutchings and J. B. Pethica, Metall. Trans. 15A (1984) 2221

[13]. A. K. Suri, R. Nimmagadda and R. F. Bunshah, Thin Solid Films 64 (1979) 191.

[14]. I. L. Singer and R. A. Jeffries, Mat. Res. Soc. Symp. Proc. 27 (1984) 667

[15]. M. A. Moore, R. C. D. Richardson, and D. G. Atwood, Metall. Trans. 3 (1972) 2485

[16]. R. G. Vardiman, R. N. Bolster and I. L. Singer, in Metastable Materials Formation by Ion Implantation, ed by S. T. Picraux and W. J. Choyke (Elsvier Science, New York, 1982) p.269

[17]. I. L. Singer, R. G. Vardiman and R. N. Bolster, J. Mater. Res. 3 (1988) 1134

[18]. S. Shrivastava, R. D. Tarey, A. Jain and K. L. Chopra, Thin Solid Films 163 (1988) 359

[19]. Karl-heinz Zum Gahr, Microstructure and Wear of Materials (Elsvier Science, Amsterdam 1987) p.62

[20]. R. Leutenecker, G. Wagner, T. Louis, U. Gonser, L. Guzman, and A. Molinari, Mat. Sci. Engr. (in press)

[21]. P. J. Wilbur and L. O. Daniels, Vacuum 36 (1986) 5

[22]. D. L. Williamson, Yi Qu, Ronghua Wei, W. S. Sampath, and P. J. Wilbur, Mat. Res. Soc. Symp. Proc. 128 (1989) 409.

[23]. W. S. Sampath, R. Wei and P. J. Wilbur, J. Metals 39 (1987) 17

[24]. data from J. P. Biersack and J. F. Ziegler

[25]. U. Gonser, Mössbauer Spectroscopy (Springer-Verlag, New York, 1975) p.1.

[26]. J. J. Spijkerman, in Mössbauer Effect Methodology ed. by Irwin J. Gruverman (Plenum Press, New York, 1971) p.85.

[27]. D. F. Fobare, Master of Science Thesis, Colorado School of Mines, Thesis number T-3009, 1986

[28]. D. Liljequist, T. Ekdahl and U. Baverstam, Nucl. Instrum. Meth. 155 (1978) 529

[29]. F. A. Deeney and P. J. McCarthy, Nucl. Instrum. Meth. 166 (1979) 491

[30]. Charles Evans and Associates, 301 Chesapeake Drive, Redwood City, CA 94063.

[31]. B. Fultz and J. W. Morris, Jr., Phys. Rev. B

34 (1986) 4486.

[32]. L. H. Schwartz and D. Chandra, Phys. Stat. Sol. 45 (1971) 201.

[33]. S. Nagy, E. Kuzmann, A. Vertes, G. Szabo,and G. Knczos , Nucl. Instrum. Meth. B34 (1988) 217

[34]. N. A. Gokcen and R. H. Nafziger, Bulletin of Alloy Phase Diagrams 8 (1987) 365.

[35]. Robert E. Reed-Hill, **Physical Metallurgy Principles**, (Pws-kent Publishing Company, Boston, 1973) p.729

[36]. C. S. Roberts, Trans. AIME 203 (1953) 191

[37]. Selected Power diffraction Data for Metals and Alloys (International Center for Diffraction Data, Pennsylvania, 1987)

[38]. R. C. Ruhl and M. Cohen, Trans. Metall. AIME 245 (1969) 241.

[39]. L. H. Schwartz and J. B. Cohen, **Diffraction from Materials**, (Springer-Verlag, New York, 1987) p.219

[40]. J. Hirvonen and A. Anttila, Appl. Phys. Lett. 49 (1985) 835

[41]. M. Piette, G. Terwagne, W. Möller, and F. Bodart, Mat. Sci. Engr B2 (1989) 189.

[42]. J. Bainbridge, D. A. Channing, W. H. Whitlow and R. E. Pendleburg, J. Phys. Chem. Solids 34 (1973) 1597.

[43]. P. Rochegude and J. Foct, Phys. Stat. Sol. A 98 (1986) 51

[44]. D. L. Williamson and L. Wang (unpublished data)

[45]. G. M. Chen, N. K. Jaggi, J. B. Butt, E.B. Yeh and L. H. Schwartz, J. Phys. Chem. 87 (1983) 5326.

[46]. A. J. Nozik, J. C. Wood, Jr., and G. Haacke, solid State Commun. 7 (1970) 1677; Solid State Commun. 8 (1970) P. viii, June 15 issue.

[47]. R. Sandström and H. Bergqvist, Scand. J. Metall. 6 (1977) 156

[48]. E. Werner, Mat. Sci. Engr. 101 (1988) 93